Structure of mitoribosome reveals mechanism of mRNA binding, tRNA interactions with L1 stalk, roles of cofactors and rRNA modifications

Vivek Singh[1,14], Yuzuru Itoh[1,2,14], Samuel Del'Olio[3,14], Asem Hassan[4,5,14], Andreas Naschberger[1,6], Rasmus Kock Flygaard[7], Yuko Nobe[8], Keiichi Izumikawa[9], Shintaro Aibara[10], Juni Andréll[11], Paul C Whitford[4,5], Antoni Barrientos[3,12,13], Masato Taoka[8], Alexey Amunts[1*]

[1] Science for Life Laboratory, Department of Biochemistry and Biophysics, Stockholm University, 17165 Solna, Sweden.
[2] Department of Biological Sciences, Graduate School of Science, University of Tokyo, 113-0033 Tokyo, Japan.
[3] Department of Molecular and Cellular Pharmacology, University of Miami Miller School of Medicine, Miami, FL 33136, United States.
[4] Department of Physics, Northeastern University, Boston, MA, 02115, United States.
[5] Center for Theoretical Biological Physics, Northeastern University, Boston, MA, 02115, United States.
[6] King Abdullah University of Science and Technology, Thuwal 23955, Saudi Arabia.
[7] Department of Molecular Biology and Genetics, Danish Research Institute of Translational Neuroscience - DANDRITE, Nordic EMBL Partnership for Molecular Medicine, Aarhus University, 8000 Aarhus C, Denmark.
[8] Department of Chemistry, Graduate School of Science, Tokyo Metropolitan University, Minami-osawa 1-1, Hachioji-shi, Tokyo 192-0397, Japan.
[9] Department of Biotechnology, Global innovation research institute, Tokyo University of Agriculture and Technology, Saiwai-cho 3-5-8, Fuchu-shi, Tokyo 183-8509, Japan.
[10] BioPharmaceuticals Research and Development, AstraZeneca, UK.
[11] Department of Medical Biochemistry and Biophysics, Karolinska Institutet, 17177, Stockholm, Sweden.
[12] Department of Neurology, University of Miami Miller School of Medicine, Miami, FL 33136, United States.
[13] Department of Biochemistry and Molecular Biology, University of Miami Miller School of Medicine, Miami, FL 33136, United States.
[14] These authors contributed equally

* correspondence: amunts@scilifelab.se

The mitoribosome translates mitochondrial mRNAs and regulates energy conversion that is a signature of aerobic life forms. We present a 2.2 Å resolution structure of human mitoribosome together with validated mitoribosomal RNA (rRNA) modifications, including aminoacylated CP-tRNA^{Val}. The structure shows how mitoribosomal proteins stabilise binding of mRNA and tRNA helping to align it in the decoding center, whereas the GDP-bound mS29 stabilizes intersubunit communication. Comparison between different states, with respect to tRNA position, allowed to characterize a non-canonical L1 stalk, and molecular dynamics simulations revealed how it facilitates tRNA transition in a way that does not require interactions with rRNA. We also report functionally important polyamines that are depleted when cells are subjected to an antibiotic treatment. The structural, biochemical, and computational data illuminate the principal functional components of the translation mechanism in mitochondria and provide the most complete description so far of the structure and function of the human mitoribosome.

The human mitoribosome translates at least 13 respiratory chain protein-coding mRNAs from the mitochondrial genome [1]. It consists of three rRNAs and at least 82 mitoribosomal proteins, 36 of which have no corresponding homologs in bacterial and cytosolic ribosomes. The mitochondrial rRNA is reduced compared to its bacterial counterpart (2,512 vs 4,568 nucleotides in *Escherichia coli*), $tRNA^{Val}$ has been incorporated as an additional constituent, and protein components are extended (~18,075 vs 7,536 residues in *E. coli*) [2]. The mitoribosomal proteins might have functional roles in mitochondria-specific aspects of translation, and therefore mutations in the corresponding genes result in cardio- and encephalomyopathies [3, 4]. However, due to the limited resolution and heterogeneity of the characterized complexes, the available models are currently incomplete, and many mitoribosomal protein key elements are described as unassigned densities [5, 6, 7, 8, 9, 10]. The existing models suggest that mitoribosomal proteins might play a role in binding mRNA, regulatory elements such as the L1 stalk are probably remodeled, and the specific mitoribosomal protein mS29, a putative GTPase is associated with inter-subunit communication. Yet, the lack of experimental data leaves open the questions of a functional involvement.

The mitochondrial rRNA is modified, and dedicated post-transcriptionally activated enzymes provide means for the regulation of gene expression and mitoribosome assembly [11]. Due to the central role of the human mitoribosome in cellular energy production, defects in rRNA modification result in fatal clinical syndromes from birth [12, 13]. Some of the bacterial counterpart modifying enzymes are missing from mitochondria, for example methyltransferases RlmA, RlmB, RmsE and pseudouridine synthase RluA, while other mitochondria-specific ones have evolved [14]. Therefore, rRNA modifications are different, and they have been identified by various experimental approaches [11, 15, 16, 17, 18, 19, 20, 21, 22, 23], furthermore recent structural studies visualized individual rRNA modifications on the mitoribosomal large (LSU) [24] and small (SSU) subunits [25, 26]. However, the entire set of modifications is yet to be quantitatively identified and visualized in the presence of bound ligands in order to enable a detailed examination of their roles. To date, the molecular mechanisms compensating for the lack of bacteria-like modifications remain unknown, as well as the modifications and the amino-acylation state of the structural $tRNA^{Val}$.

Mitoribosomes are also linked to age-related diseases that are associated with decline in mitochondrial function and biogenesis [27, 28, 29, 30]. Aging-related pathological changes can be inhibited by polyamine consumption [31, 32], which also has anti-inflammatory effects in mouse models *in vivo* [33]. Polyamines have been shown to be essential for mammalian cell differentiation and proliferation through their impact on translation dynamics [34, 35]. However, no polyamine biosynthetic pathways within mitochondria have been found, and their role in mitochondrial physiology remained unknown. Whether mitoribosomes might be related to these phenomena and associated with cellular senescence via polyamines needs to be explored.

To address these issues, we combined high resolution structural studies of mitoribosomal complexes with mass spectrometry based quantitative RNA analysis, biochemistry, and molecular dynamics simulations.

112 **Structure determination**

113 To produce a 2.2 Å overall resolution map of the mitoribosome, we collected five separate cryo-
114 EM datasets. Selected monosome particles were subjected to per-particle defocus, beam-tilt and
115 per-particle astigmatism correction, followed by Bayesian polishing [36, 37]. The data was then
116 sorted into 86 optics groups based on acquisition areas followed by beam-tilt, magnification
117 anisotropy and higher order aberration correction [38]. A final set of 509,691 particles yielded a 2.2
118 Å map. The local resolution was further improved by performing masked refinements around
119 different regions of the monosome. In addition, we obtained a 2.6 Å resolution map in the
120 presence of mRNA and three tRNAs in the classical state, and 3.0 Å resolution map with two
121 tRNAs in the hybrid state (Supplementary Figs. 1 and 2). The improved resolution allowed
122 building the most complete available model of the mitoribosome, including several key protein
123 extensions involved in tRNA binding (Fig. 1a). The presence of mRNA on the mitoribosome
124 further enabled modeling 32 of its residues, which we then used to trace mitochondria-specific
125 elements involved in mRNA binding and put the rRNA modifications in a functional context
126 (Fig. 1b).
127 To provide a description of the conformational changes associated with tRNA movement, we
128 next focused efforts on modelling the L1 stalk. Thus, we merged particles containing tRNA in
129 the E-site and through partial signal subtraction [39] and obtained a 2.9 Å resolution map of the
130 region, enabling model building of the L1 stalk (Supplementary Fig. 1). We then used this model
131 to perform molecular simulations of the complete ribosome with tRNAs.

132

133 **rRNA and protein modifications, aminoacylated tRNA^{Val}, polyamines**

134 On the rRNA level, the quality of the map allowed the modeling of 13 rRNA modifications, of
135 which 6 are mitochondria specific compared to *E. coli* [21]. All the rRNA modifications
136 were validated by a tailored quantitative method of Stable Isotope-Labeled riboNucleic Acid as
137 an internal Standard (SILNAS) [40] (Supplementary Figs. 3,4). The mitochondria specific
138 modifications include base methylations m^{5}U1076, m^{5}C1488 in the SSU; m^{1}A2617 in the LSU;
139 and m^{1}A9, m^{2}G10 and ψ39 in the tRNA^{Val} incorporated in the central protuberance (CP) [41, 42, 43]
140 (Fig. 1b). In the map, methylations of rRNA were identified by systematically examining the
141 density map for the presence of unmodeled densities continuous with the base or sugar moieties
142 of rRNA residues (Fig. 2). Identity of the two high-occupancy pseudo-uridines was established
143 based on the presence of a structured water molecule within hydrogen-bonding distance from the
144 N5 atom.

145 The tRNA^{Val} modifications are consistent with the previous mass-spectrometry data on isolated
146 mitochondrial tRNAs from a general pool [44] (Fig. 3). The density further revealed that the
147 tRNA^{Val} incorporated in the CP is amino acylated (Fig. 2a). In the structure, ψ39 of tRNA^{Val}
148 contributes to the conformation of the anticodon arm, which contacts uL18m, mL38, mL40 and
149 mL48 (Fig. 3a). In addition, two methylated residues, m^{1}A and m^{2}G, are observed at the
150 positions 9 and 10, respectively in the D arm (Fig. 3a). m^{1}A9 is stacked between G45 and A46

151 and forms a base triple with the second base pair (C11:G24) of the D stem. On the other hand,
152 m^2G10 is stacked between C11 and A26 and forms the first base pair (m^2G10:C25) of the stem,
153 which further interacts with G45 to be a base triple. These methylations facilitate the stacking
154 and hydrogen bonds among bases, and thereby contribute to the conformation of the D arm,
155 which contacts uL18m and mL38 (Fig. 3a-c). The terminal A76 has a base-specific interaction
156 with Q175 of mL46 and together with Valine is stacked with F165 and F215 (Fig. 3d).
157 A notable feature of the cryo-EM map is the presence of continuous tubular densities associated
158 with rRNA that we assigned as polyamines, justified by the electrostatic and hydrogen-bonding
159 interactions at the amine groups (Supplementary Fig. 5). Thus, in addition to a previously
160 assigned spermine (SPM) [45], we detected one triamine spermidine (SPD) in the SSU, and a
161 diamine putrescine (PUT) and three SPDs in the LSU. The identified polyamines are bound to
162 negatively charged rRNA where mitochondria specific changes occur, providing required
163 structural support (Fig. 4; Supplementary Fig. 5). For example, SPD3301 in the LSU fills the
164 formed space of a shortened mitoribosomal protein uL2m, which has undergone reduction in the
165 human mitoribosome. SPD3303 is tethered to uL3m, where a bacterial counterpart has a
166 signature Q150 methylation, therefore replacing the post-translational modification. The PUT is
167 found in the exit tunnel upper region of uL22m hairpin.

168 Finally, the model contains seven protein modifications; three iron-sulfur clusters, one of which
169 is coordinated by uL10m and mL66 and reported here for the first time, and a molecule of
170 nicotinamide adenosine dinucleotide (NAD) reported previously [26, 45, 46] (Fig. 1b, Supplementary
171 Table 1). We also identified a disulfide bond in one of the two redox active cysteine pairs in
172 mS37 (CHCHD1) (Fig. 2) that is oxidized in the intermembrane space during mitochondrial
173 import, representing a quality control mechanism [47].

174

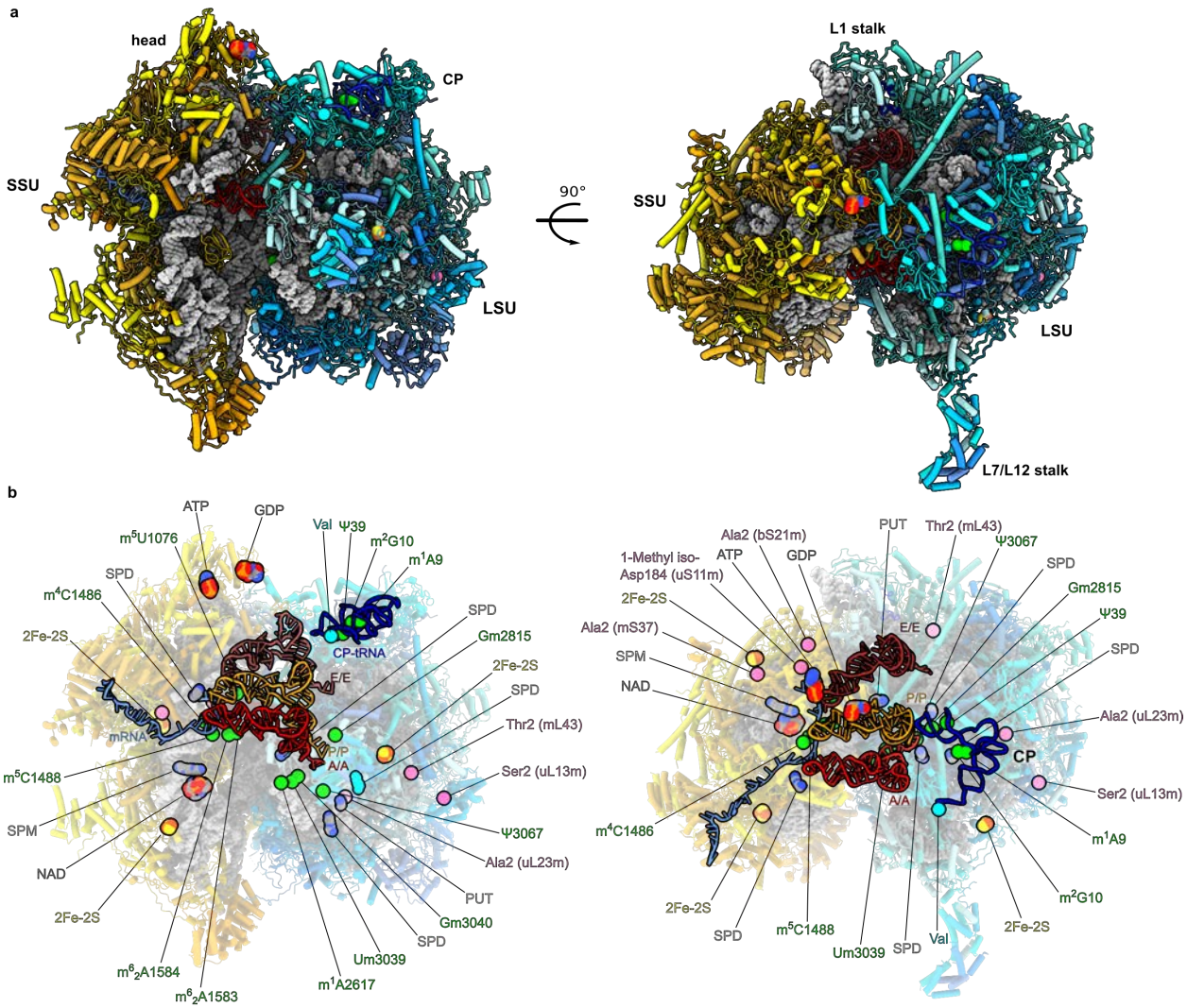

Fig. 1: Structure of the human mitoribosome. a, Overview of the 2.2 Å resolution model with mRNA and tRNAs. Proteins are shown as cartoons colored in blue for the LSU and yellow for the SSU. The rRNA is shown as grey surface. Newly identified features are shown as spheres. **b,** The newly identified cofactors and modifications are indicated against background of translucent rRNA and proteins with tRNAs and mRNA shown in cartoon. We observe 13 rRNA modifications (green), 7 protein modifications (pink), 3 iron-sulfur clusters (red-yellow), guanosine diphosphate (GDP), adenosine triphosphate (ATP), NAD, SPM, 4 SPDs and PUT.

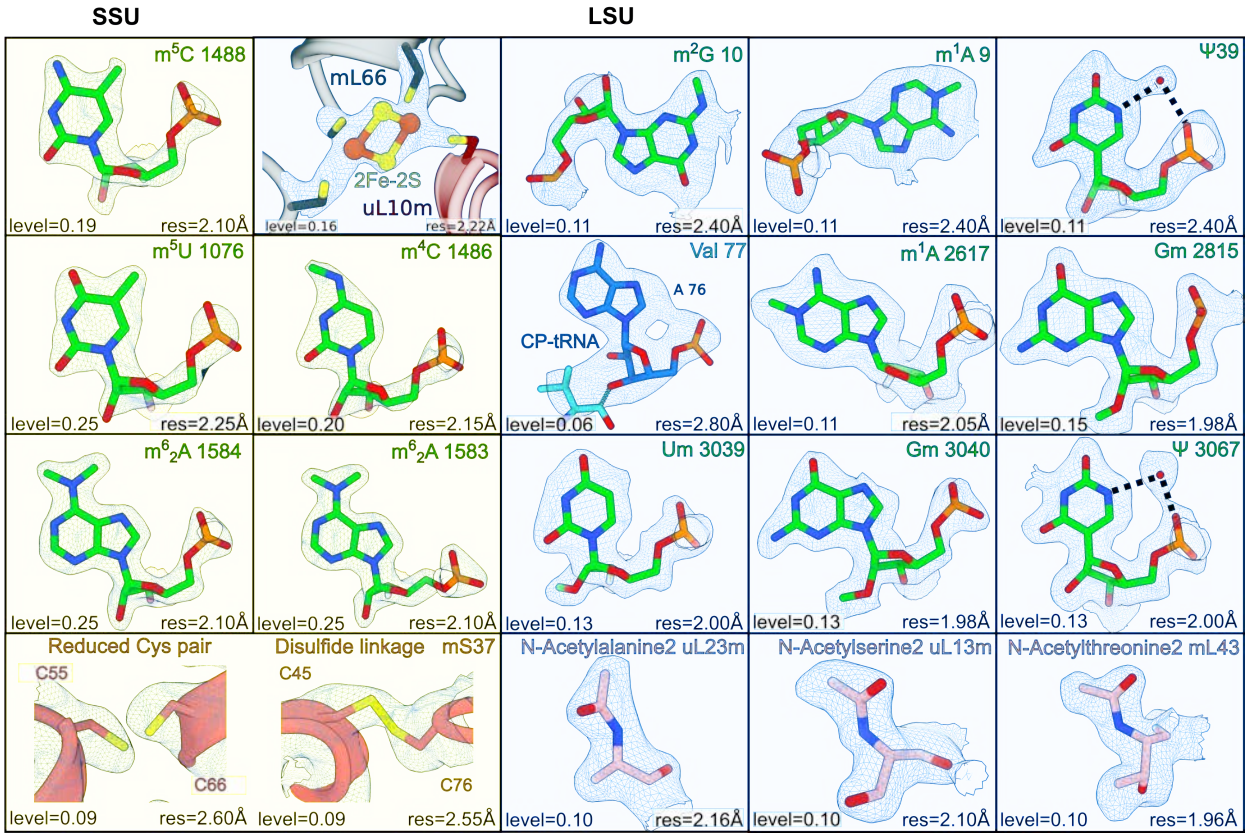

Fig. 2: High resolution features. Modified rRNA residues and disulfide-linked or reduced cysteine residues of mS37 in the SSU (yellow background). Modified rRNA and protein residues, and 2Fe-2S cluster in the LSU (cyan background). Their corresponding densities in the 2.2 Å map are shown as mesh at indicated threshold (bottom left) and local resolution (bottom right) levels.

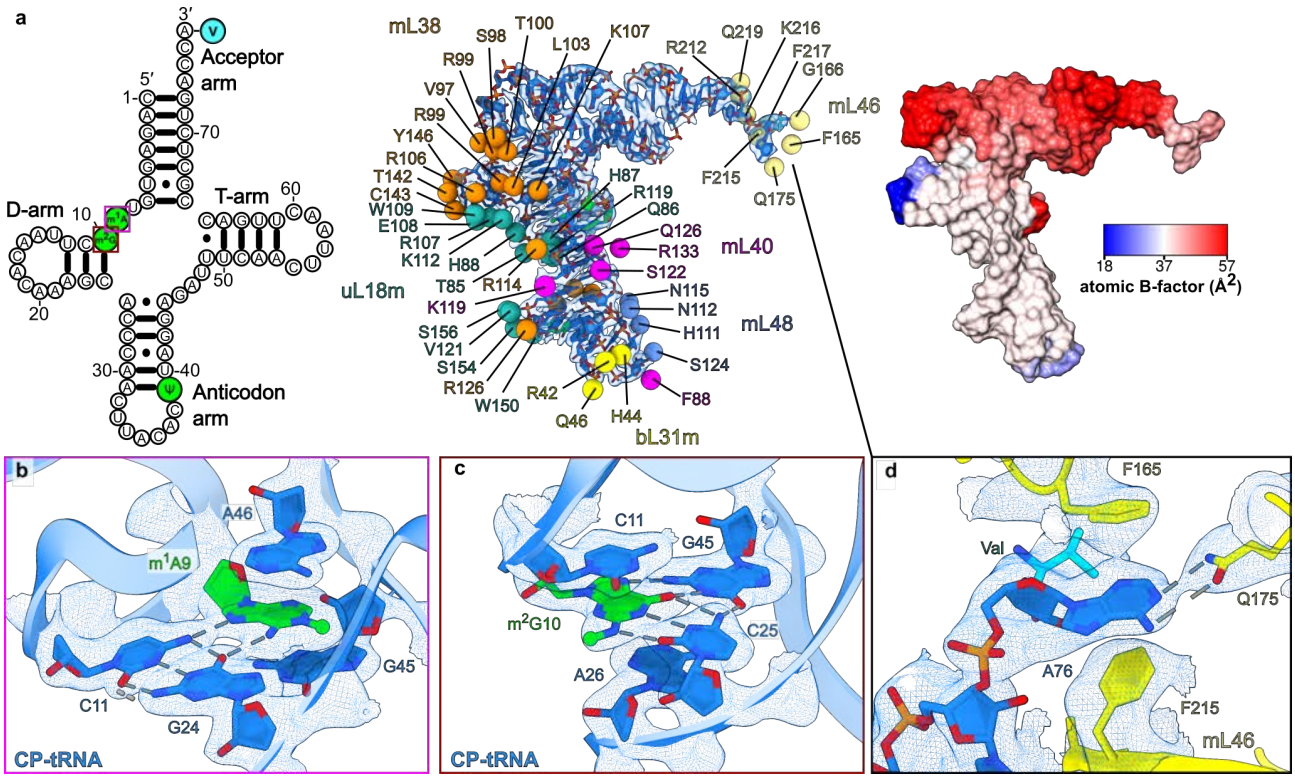

Fig. 3: Interactions and post-transcriptional modifications in CP-tRNA of the mitoribosome. a, CP-tRNA^{Val} (left to right) secondary structure diagram with modified nucleotides (green) and valine (cyan) highlighted, protein-contact map, *B*-factor representation. **b,c,** Interactions of the modified m^{1}A9 and m^{2}G10 nucleotides of CP-tRNA^{Val}. **d,** Interactions of A76 and V77 of CP-tRNA^{Val} with mL46. The cryo-EM density map is displayed for panels b-d (consensus map) as blue mesh. Panels (b) and (c) are related to panel (a) on the left by colored boxes.

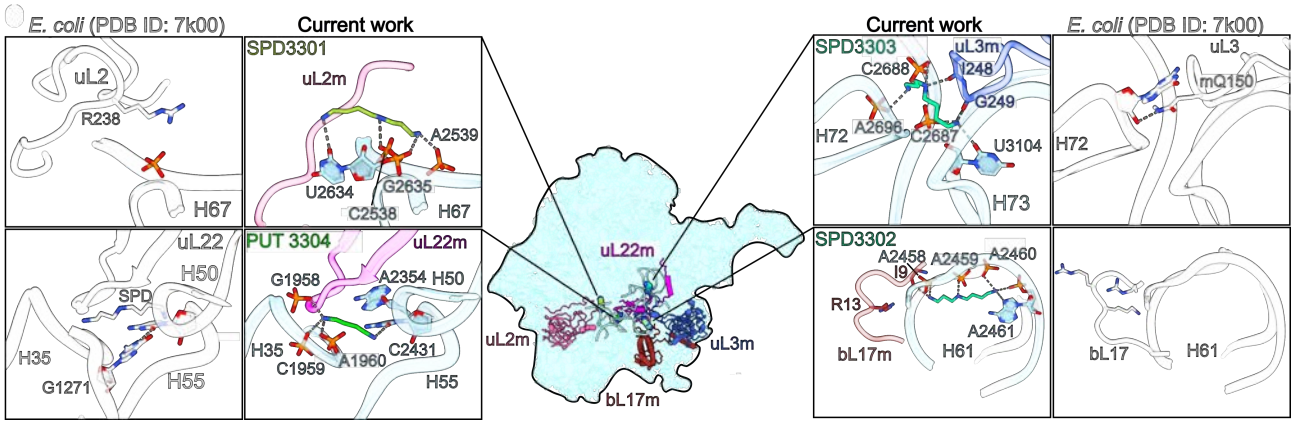

Fig. 4: Polyamines functionally compensate for rRNA and protein alterations. Central inset shows positions of polyamines and interacting rRNA and proteins in the LSU. For each polyamine, its environment and interacting partners are shown in zoom-in panels with *E. coli* counterparts [48] (white) for comparison.

203

204 **Initial binding of mRNA involves Y-N-C-Y motif coevolved with mS39**

205 The modulation of a stable mitoribosomal complex allowed us to resolve the mRNA path and
206 investigate mitoribosome-specific components involved in mRNA recognition (Fig. 5,
207 Supplementary Fig. 6, Supplementary Video 1). It engages seven helical repeats of mS39 with
208 specific contacts within a prominent positively charged groove (Fig. 5a). Particularly, a
209 pyrimidine ring of the mRNA nucleotide in position 25 is stacked between H489 and R524 and
210 interacts with S490 of mS39 (Fig. 5a,b). Hydrogen bonding between the side chain of R377 of
211 mS39 and nucleotide 27 favors cytosine over uracil because the protonated N3 of a uracil would
212 partially clash with the protonated Nη of R377. R343 of mS39 forms a hydrogen bond with the
213 pyrimidine ring of nucleotide 28. Thus, the structure reveals a binding motif: 25 pyrimidine (Y),
214 27 cytosine (C), 28 pyrimidine (Y) (Fig. 5a,b). Bioinformatic analysis showed that the Y-N-C-Y
215 motif is enriched in mitochondria and distributed over the entire length of each of the 12 open
216 reading frames in the guanine-rich heavy DNA strand, suggesting a co-evolution of the
217 mitochondrial DNA and the mitoribosome (Fig. 5c, Supplementary Fig. 7). The only mammalian
218 protein-coding gene with a reduced frequency of the Y-N-C-Y motif is the *MT-ND6* that is on
219 the light strand and codes for an 18-kDa subunit of complex I. The expression of the ND6
220 mRNA is unique, as it requires an auxiliary factor FASTK to generate the mature form,
221 suggesting a dedicated regulatory mechanism [49].

222 The most 5' contact between mRNA and mS39 is ~50 Å from the channel entrance, and by
223 following the mRNA density toward the decoding center, we identified six specific
224 mitoribosomal proteins that are important for mRNA recruitment, channel opening, and precise
225 alignment of the message for translation in the decoding center. In our structure, the Y-N-C-Y
226 motif forms a ~100° turn (kink-1) in the mRNA midway through mS39 (Fig. 5a and
227 Supplementary Video 1). After the kink, the N-terminal mitochondria-specific extension of
228 uS5m supports the path of mRNA over a distance of ~60 Å, involving a unique N-terminal
229 polybasic stretch of 14 residues 111-124 (KKGRGKRTKKKKRK) together with R237 and
230 K239 (Fig. 5d, Supplementary Video 1, Supplementary Fig. 6). From the side of the SSU head,
231 mS35 provides potential stabilizing electrostatic interactions to mRNA with N-terminal residues
232 K46 and K49 (Fig. 5e,f). This mitochondria-specific extension of uS5m structurally replaces
233 bacterial bS4 and uS3-CTD that interact with mRNA (Supplementary Fig. 6) and confer RNA
234 helicase activity on the bacterial ribosome [50]. Just before the channel entry, the binding of
235 mRNA induces a conformational change of the N-terminal extension of uS9m that contacts the
236 mRNA nucleotide at position 15 via the backbone of V55 (Fig. 5e,g; Supplementary Video 1),
237 which in the absence of mRNA blocks the entrance to the decoding center [51]. Thus, uS9m exists
238 in a closed conformation in the absence of mRNA, and upon mRNA threading, a conformational
239 change in uS9m allows the passage (Fig 5h).

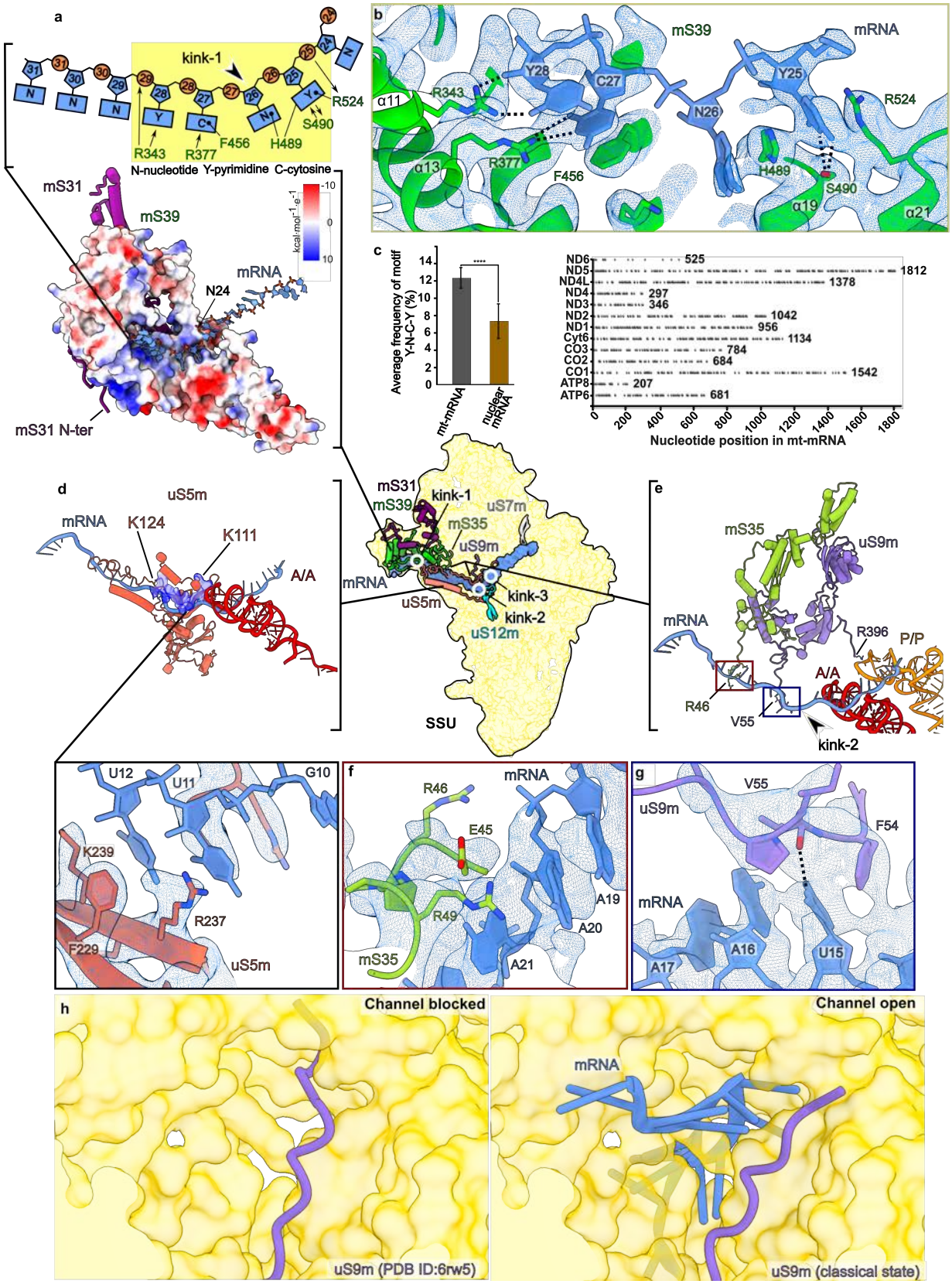

Fig. 5: Specific protein elements involved in mRNA binding.

242 **a,** Electrostatic coulomb potential surface representation of the model shows a positively charged
243 groove (blue) on mS39 that accommodates the mRNA. N-terminal loop of mS31 interacts with
244 mS39. Y-N-C-Y motif and its interactions with mS39 residues are depicted as a schematic.
245 Position of kink-2 is marked. **b,** Interactions of the Y-N-C-Y motif with mS39 and density map
246 (mesh). Protein mS31 has been removed for clarity. **c,** Average percentage frequency of Y-N-C-
247 Y motif (left) with +/- standard deviation for mitochondrial mRNAs (excluding ND6; dark grey
248 bar) and nuclear mRNA (brown bar). P-value (<0.0001) calculated by Welch's unpaired t-test.
249 Positions of the Y-N-C-Y motif in the mt-mRNAs are shown as discs (right) to depict its
250 distribution along the mt-mRNA sequences. The total number of residues for each mt-mRNA is
251 indicated. **d,** Overview of uS5m showing a region of contact with mRNA. The polybasic stretch
252 111-124 along the mRNA is colored by electrostatic potential. Interacting residues between
253 uS5m and mRNA are shown with the local density map. **e,** Interactions of mS35 and uS9m with
254 mRNA at the channel entry and the P-site. **f,** R46 and R48 of mS35 potentially interact with the
255 mRNA backbone, and the density suggests flexibility of the side-chains. **g,** uS9m forms stacking
256 and hydrogen bonding interactions with mRNA position 15 via F54 and V55, respectively. **h,**
257 uS9m N-terminus (purple cartoon) adopts alternative conformations that result in mRNA channel
258 blocked or open states regulating mRNA access to the SSU (gold surface).
259
260 **mL40 N-terminal tail stabilizes the A- and P-site tRNAs and decoding interactions**
261 We then examined the role of mitoribosomal proteins in the mRNA alignment. The structure
262 shows that to enter the SSU channel, the mRNA must be kinked again (kink-2), and in the A-site
263 the nucleotide at position 9 is stabilized by uS12m (Supplementary Fig. 8). Here, a conserved
264 K72 side chain forms a salt bridge with the phosphate of nucleotide 9 (last nucleotide in the A-
265 site codon). At the same time, *cis*-proline P73 (Supplementary Fig. 8) coordinates two potassium
266 ions, one of which directly coordinates 2´O of nucleotide 9 (Supplementary Fig. 8,
267 Supplementary Video 1) and stabilizes the decoding center. The densities identified as two
268 potassium ions have been observed previously, but modeled as Mg^{2+} (PDB 4V51) [52] or waters
269 (PDB 7K00) [48, 52]. However, they have been experimentally identified as K^{+} by long wavelength
270 X-ray diffraction analysis (PDB 6QNR) [53], which agrees with our assignment (Supplementary
271 Fig. 8).
272 Next, between the A- and P-site, the map reveals a third kink in the mRNA (kink-3), which is co-
273 localized with a 35-Å long density extending from the CP in between the two tRNAs (Fig. 6a,
274 Supplementary Fig. 9a) that could not be previously interpreted. We identified it as a positively
275 charged N-terminus of mL40 with the terminal backbone amino group of S47 forming a salt
276 bridge with the backbone phosphate of the mRNA at position 7 in the A-site (Fig. 6a,
277 Supplementary Fig. 9b), and the interaction is further stabilized via a magnesium ion coordinated
278 by the phosphate of G1485. In addition, the hydroxyl group of S47 interacts with the mRNA
279 nucleotide base at position 6 in the P-site (Fig. 6a, Supplementary Video 1), although the
280 contacts are likely to be flexible. Moreover, the base orientation allows any nucleotide to interact
281 with S47 (Supplementary Fig. 9c). The concept is analogous to the cytosolic ribosome that

engages uS19 for tRNA stabilization and mRNA interactions in the decoding center [54] (Fig. 6b). The presence of four lysine residues 52-55 (Fig. 6a, Supplementary Fig. 9b), might suggest that mL40 contributes to balancing the charge between the A- and P-tRNAs. Together with R51, which forms salt bridges with A1560 and C1561 in h44, the positively charged patch compensates for the negative RNA charges accumulated in that region (Fig. 6a, Supplementary Fig. 9b, Supplementary Video 1). Further in the P-site, we observe a well-resolved density showing the conserved C-terminal R396 of uS9m interacting with the anticodon loop of the P-site tRNA (Supplementary Fig. 9d). Finally, in the E-site, uS7m residues G164-165 further contribute to mRNA stabilization (Supplementary Fig. 9e). Thus, mitoribosomal proteins play a role in mRNA binding.

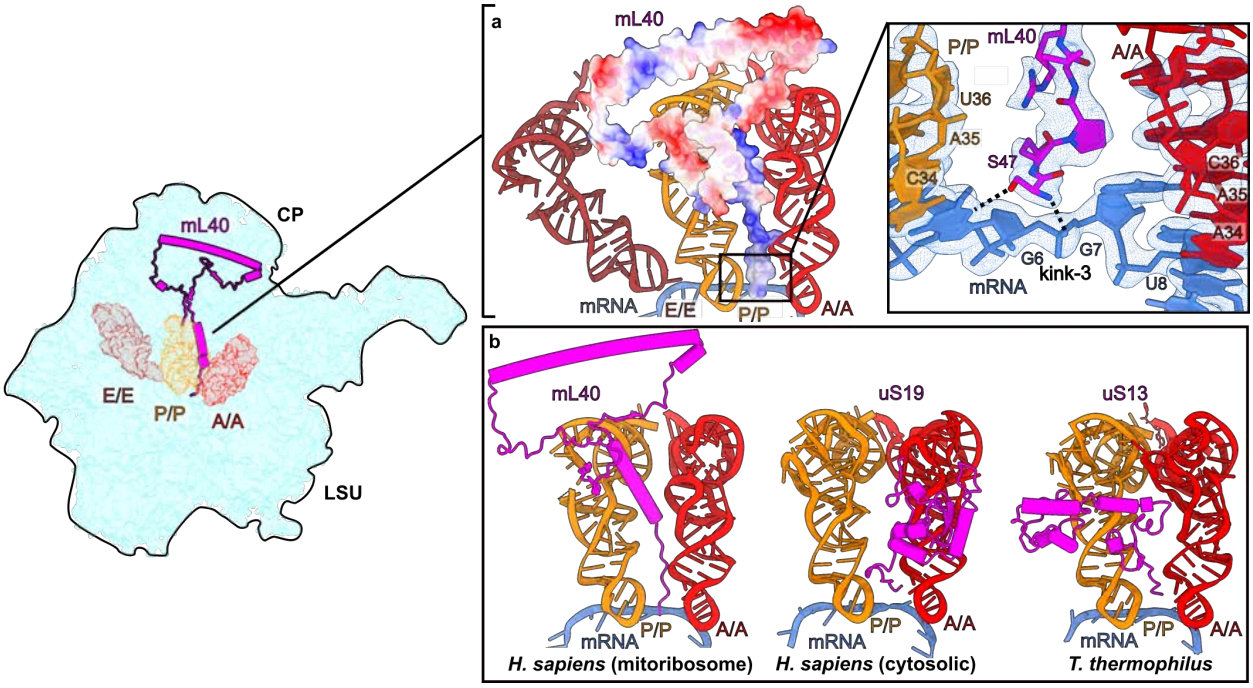

Fig. 6: Analysis of mRNA binding in tRNA sites. a, Interactions of mL40 (shown with electrostatic potential of the model) with mRNA between A/A- and P/P-tRNAs. Hydrogen bonds G6 base and G7 phosphate are shown as dashed lines. **b,** Comparison of mL40-tRNA interaction (left) with those of uS19 (middle) and uS13 (right) in human cytosolic [54] and *T. thermophilus* ribosome [52], respectively.

mRNA alignment in the decoding center and rRNA modifications

In the decoding center, the universally conserved G902 is in *anti* conformation, while A1557 and A1558 are flipped out from h44 to interact with the A-site codon:anti-codon helix in the canonical manner [55, 56] (Supplementary Fig. 10). A well-resolved density, combined with the mass-spectrometry SILNAS [40, 57, 58] approach further allowed us to validate the complete set of the rRNA modifications, including six mitochondria specific, and propose a role in stabilizing the decoding center (Fig. 5, Supplementary Figs. 4 and 5). Close to the decoding center, the residue G899 was recently shown to interact with streptomycin in human mtSSU [45]. Its

methylated to m^7G527 in *E.coli* (Supplementary Fig. 10) and this modification partly contributes to streptomycin sensitivity [59]. In the P-site, two base-methylated nucleotides m^4C1486 and m^5C1488 flank the base triple C1487:A1564:U1563 by stabilizing the stacking interactions (Fig. 5a,b). The orientation of N^4-methylated m^4C1486 towards mRNA is conserved with respect to *E. coli*, where the corresponding residue is also 2'-O methylated ($m^4Cm1402$) (Supplementary Fig. 10). m^4C1486 together with C1487 interacts with the phosphate group of the last nucleotide in the P-site mRNA codon via hydrogen bonds (Fig. 5a,b). Further, phosphate group of m^4C1486 coordinates a magnesium ion, which stabilizes a conserved kink of the mRNA between A- and P-sites (Fig. 7a). In contrast to the *E. coli* P-site, U1563 does not have an N^3-methylation (m^3U1498 in *E. coli*) (Supplementary Fig. 10). This lack of N^3-methylation allows U1563 together with C1487 to form a water mediated interaction with the P-site codon (Fig. 7a,b). Further, the conserved dimethylated residues, $m^6{}_2A1583$ and $m^6{}_2A1584$ orient the nucleotide U1563 such that the ribose of U1563 forms a hydrogen bond to a phosphate group of the second nucleotide in the P-site mRNA codon, while the phosphate of U1563 forms a hydrogen bond with the ribose on the first codon nucleotide (Fig. 7b). The two dimethylated nucleotides facilitate A1080 positioning for the 2′-OH to hydrogen bond with N3 of m^5U1076. This together with methylation of m^5U1076 contributes to the stability of h24 loop that interacts with the P-tRNA anticodon stem at position 38 via A1078 (Fig. 7a,b).

In the A-loop of H92, there are two 2′-O-methyl modified nucleotides Um3039 and Gm3040. The 2′-O-methyl of Um3039 sterically positions the bases of Gm3040 and U3041 to form interactions with the nucleotides C75 and C74 of the A-tRNA, respectively (Fig. 7c,d). The 2′-O-methyl of Gm3040 present in the cytosolic but not bacterial ribosome and interacts with the base of A3069 to stabilize the conformation of Gm3040. Furthermore, the bacterial counterpart rRNA that interacts with A-tRNA (C75) is G:C, whereas in our structure it's A:U (3069:2994) that is less stable, and thus stabilized by the mitochondria-specific methylation of Gm3040 and base-pairing interactions with ψ3067 (Fig. 7d). In the LSU, mitochondria-specific m^1A2617 positions U2614 into a wedged interaction (Fig. 7e). Surprisingly, there is only weak sugar puckering for m^1A2617 (Fig. 2a). It bears a partial positive charge at N1 and interacts with U2649 of H61. The interactions mediated by m^1A2617 potentially contribute to the structuring of H71 loop that participates in an intersubunit bridge shares an interface with the A-loop (Fig. 7e). The universally conserved Gm2815 in the P-loop forms Watson-Crick base pairing with C75 of P/P-tRNA, similar to the interactions of Gm3040 of the A-loop (Fig. 7f).

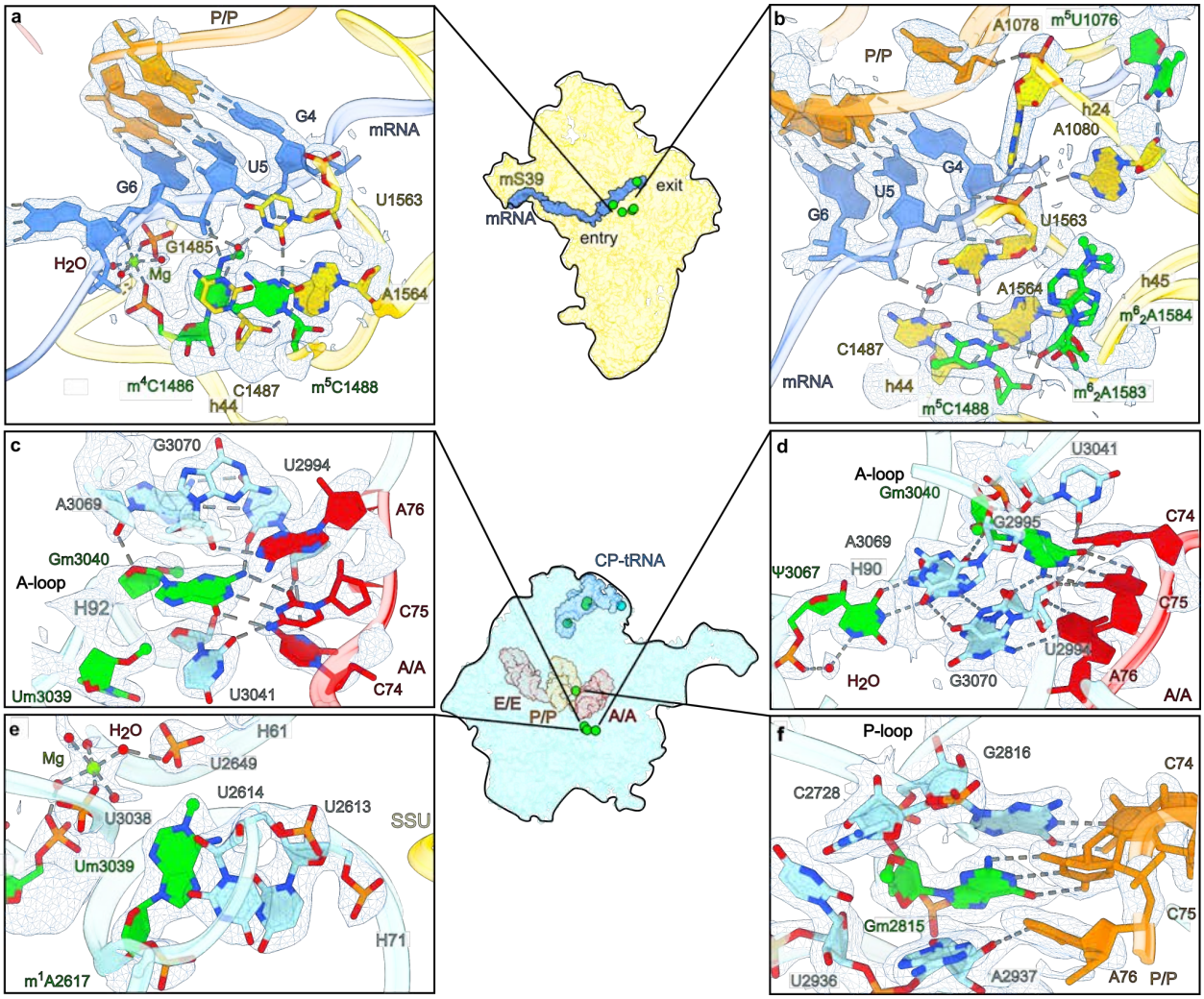

Fig. 7: Post-transcriptional modifications in functional centers of the mitoribosome. **a,** Base-methylated m^4C1486 and m^5C1488 and the interactions at the P-site mRNA codon. **b,** The dimethylated $m^6{}_2A1583$, $m^6{}_2A1584$ and base-methylated m^51076 facilitate interactions with mRNA codon and P-tRNA. **c,** 2′-*O*-methyl modified Um3039 and Gm3040 lead to interactions with A-tRNA. **d,** Gm3040 and Ψ3067 contribute to the interface with the A-tRNA. **e,** m^1A2617 contributes to a stabilization of inter-subunit bridge and the A-loop. **f,** Gm2815 base-pairs with P-tRNA. Cryo-EM density map (A/A P/P E/E state) is displayed as a blue mesh.

Structure of the mitoribosomal L1 stalk reveals its unique protein features

To investigate whether mitoribosomal proteins might also have influence on tRNA rearrangement in the E-site, we aimed to perform molecular simulations of the mitochondrial L1 stalk. Therefore, we modeled the complete structure of the L1 stalk, which relies on mitochondria specific protein elements. In the structure, the E-tRNA is stabilized via mitochondria-specific protein elements of the C-terminal domain of uL9m and 33-residue N-terminal extension of uL1m (Fig. 8a,b). The orientation of the uL9m C-terminal domain adopts a

355 previously unseen folded conformation involving a ~75° rotation towards the E-tRNA (Fig. 8c).
356 This unexpected conformational difference is facilitated by the C-terminal helix in the extension
357 that reaches and contacts the non-base-pairing part and the distal short hairpin of the rRNA H76
358 (Fig. 8d). The resulting projection of uL9m towards the ribosomal core reduces the distance
359 between the central helix and the C-terminus of uL1m from ~70 to only ~30 Å. This distance is
360 spanned by the uL1m mitochondria-specific extension that forms direct contacts with the central
361 helix of uL9m (Fig. 8d-f). Therefore, our model of the L1 stalk establishes a tertiary
362 mitoribosomal complex uL9m:uL1m:rRNA-H76, where uL9m acquires a new functional role.
363 From the opposite side, the mitochondria-specific mL64 approaches the T-arm through its long
364 C-terminal helix extending to the tRNA binding sites.

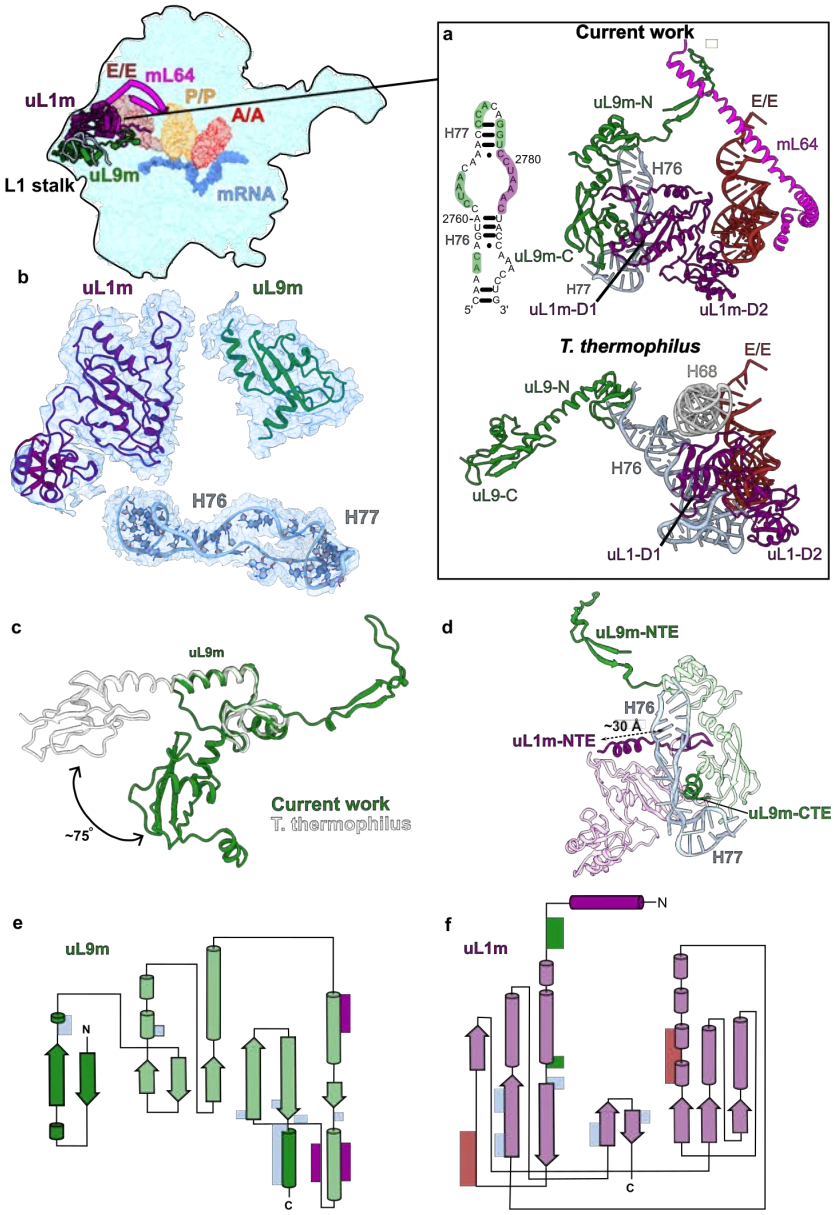

365
366 **Fig. 8: Structural features of the L1 stalk and interactions with tRNA.**

367 **a,** The L1 stalk components uL9m (green), uL1m (purple) rRNA helix H76-77 (residues 2757-
368 2790, light blue), as well as mL64 (magenta) interact with E/E-tRNA. The structure and
369 interactions are different from *T. thermophilus* (PDB ID: 4V51) [52] **b,** Components of the L1 stalk
370 modeled into their respective densities (shown as mesh). **c,** Comparison of uL9m conformation
371 with that of *T. thermophilus* uL9 (white PDB ID 4V51). **d,** Model of uL1m stalk with uL9m in
372 green and uL1m in purple, highlighting mitochondria-specific protein elements. **e,** 2D diagram of
373 uL9m showing interactions with E/E-tRNA (brown bars), rRNA (light-blue bars), uL1m (dark-
374 blue bars). Conserved regions are shown in light and mitochondria-specific in dark colors. **f,** 2D
375 diagram of uL1m color-coded as in panel d.
376

377 **Recognition of tRNA by the L1 stalk and intersubunit communication**

378 We next used an all-atom structure-based model [60, 61] to simulate hundreds of transitions of the
379 tRNA from the P site to P/E state (Fig. 9a,b; Supplementary Video 2). To isolate the influence of
380 uL1m and mL64, we compared the dynamics with four variants of the model (Fig. 9c; see
381 Methods): 1) baseline model; 2) truncated mL64 (ΔmL64) with C-terminal region starting with
382 Q112 being removed to prevent steric interactions between mL64 and EE-tRNA without
383 disturbing the rest of the protein.; 3) modified uL1m (ΔuL1m) where stabilizing interactions
384 between uL1m and P-site-tRNA are scaled down compared to the baseline model (values
385 available in methods); 4) both ΔmL64 and ΔuL1m modifications are included (see methods
386 section for details of the models). Using these models, we simulated 1066 spontaneous (non-
387 targeted) transitions between the classical (A/A P/P) and hybrid (A/P P/E) states, which include a
388 ~40 Å displacement of the P-tRNA and spontaneous rotation of the SSU (Supplementary Video
389 2). A mechanistic insight from these calculations is that mL64 imposes strict limits on the
390 pathways that are accessible to tRNA, which thereby favors a specific sequence of
391 conformational substeps during P/E formation (Fig. 9d-g). As a result, mL64 ensures that the
392 tRNA is properly positioned and may reliably engage uL1m as the tRNA approaches the E site.
393 The structure also shows that due to the different type of tRNA binding, no base pairs are formed
394 between the E/E-tRNA and mRNA, unlike those found in bacteria [62] (Supplementary Fig. 9e).
395 Instead, the protein uS7m undergoes a conformational change in which residues G164-165
396 directly contact the mRNA and stabilize its binding (Supplementary Fig. 9e, Supplementary
397 Video 1). Thus, upon each translation step, a tRNA is recognized in the E-site and escorted from
398 the mitoribosome without involving rRNA, which is strikingly different from bacterial and
399 cytosolic counterparts.

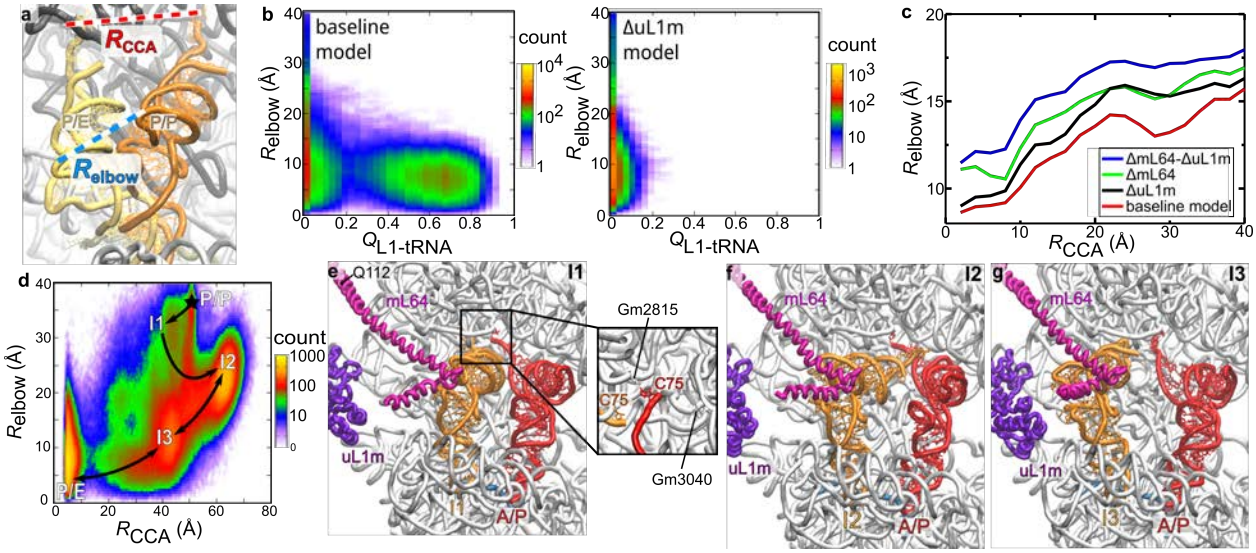

Fig. 9: Simulations of P/E formation reveal the influence of mitochondria-specific proteins. **a,** Distances R_{elbow} and R_{CCA} are used to describe the position of the tRNA during P/E formation. **b,** Probability distribution as a function of P-site tRNA elbow position (R_{elbow}) and the fraction of uL1m-tRNA contacts ($Q_{L1\text{-}tRNA}$) relative to those formed in the E/E state, calculated from simulations that used the baseline model (left). When uL1m-P-tRNA contacts are attenuated (ΔuL1m model; right), $Q_{L1\text{-}tRNA}$ remains low, consistent with a lack of uL1m binding. **c,** In simulations of P/E formation, perturbations to uL1m and/or mL64 (models ΔuL1m, ΔmL64, and ΔmL64-ΔuL1m models) lead to a wider range of tRNA elbow positions and longer timescales for P/E formation. The narrower range of pathways accessed with the complete/baseline model leads to a lower average value of R_{elbow} as a function of the tRNA CCA position R_{CCA},showing how the corridor favors a process where the elbow motion precedes CCA movement. **d,** Probability distribution (327 simulated events) as a function of elbow and 3′-CCA position reveals distinct intermediates during P/E formation. Representative structural snapshots of I1-I3 are shown in panels e-g. **e**, Intermediate I1 is associated with a small displacement of the tRNA elbow and CCA tail toward the E site. **f,** In order to reach I2, the tRNA elbow is displaced by an additional ~10Å, where it it confined by contacts with mL64. **g,** mL64 then guides the tRNA elbow towards the E site, allowing it to adopt I3. After reaching I3, a final ~40Å displacement of the CCA tail results in adoption of the P/E conformation.

Mitoribosome function is independent of mS29 GTPase activity, but GDP stabilizes intersubunit communication

For each translation step, the movement of mRNA:tRNA is also accompanied by the SSU head swiveling, but it has remained an open question whether intrinsic GTPase activity of mS29 (also known as death-associated protein 3, DAP3) is coupled to the process [63, 64]. We now resolve it by analyzing the structure in two different conformations combined with structure-based mutagenesis and biochemical analysis (Fig. 10, Supplementary Fig. 11a-c). Particularly, we performed site-directed mutagenesis targeting the previously reported nucleotide-binding site [2, 63]

428 and found that the mutant K134A, which based on the structure would affect the nucleotide
429 binding, appears to be dispensable for mitoribosomal function (Supplementary Fig. 11a,b).
430 Recently, another putative binding site has been proposed, formed with residues 173, 177, 208,
431 209, 210, 238, 242, 245, 291, 292, 295 [45, 46] (Fig. 10a,b, Supplementary Fig. 11d), and our map at
432 the local resolution of 2.65 Å suggests the presence of GDP in that site. To address the functional
433 relevance of the GDP, we compared it with the SSU structure in the presence of a
434 nonhydrolyzable analog GMPPNP [45] (Fig. 10a,b). It showed a very similar global architecture of
435 mS29, implying that no net conformational change is involved upon GTP hydrolysis (Fig.
436 10a,b). Furthermore, there is no loss of interactions of mS29 with its binding partners in the SSU
437 head (Fig. 10b). Together, the data suggest that the GTPase activity is not coupled to the
438 translation cycle and the related SSU head swiveling.
439 We next used structural and biochemical analysis to identify the role of the GDP. We compared
440 the interactions of mS29, which is the signature protein of the SSU head with the CP between
441 our classical (2.6 Å resolution) and hybrid (3.0 Å resolution) structures. In the classical state,
442 they are extensive and manifest through three contact sites. Site-1 and -2 are formed between
443 GDP-associated region and the respective mL46 helices α2 and α3 extending from the CP.
444 Contact site-3 is formed with mL48 β-turn protruding into the intersubunit space. Upon subunit
445 ratcheting, in the hybrid state mS29 shifts resulting in disruption of contact site-3. Further, the
446 mS29 β-hairpin 208-216 (stabilized by GDP) that formed contact site-2 in the classical state
447 switches in the hybrid state and remains the only inter-subunit bridge in the dimeter of 50 Å (Fig.
448 10c, Supplementary Fig. 11e). To assess the role of GDP binding in translation, we generated
449 cell lines stably expressing mS29 mutants to disrupt the GDP binding site (Fig. 10d-g,
450 Supplementary Fig. 11a-c).
451 Expression of the double mutants R177A/K245A or R177A/K295A, which target residues
452 interacting with the phosphate groups of GDP, led to reduced levels of mitochondrion-encoded
453 proteins and cellular respiration (Fig. 10d-g, Supplementary Fig. 11c), suggesting a stabilizing
454 role for GDP in this pocket. The R177A/K245A mutation shows only a tendency toward a more
455 stringent effect on mitochondrial protein synthesis than the R177A/K295A mutation in our short
456 15 min pulses. However, the effect is significant when looking at the steady-state levels of
457 mtDNA-encoded proteins. (Fig. 10d,e). Interestingly, the double mutant R177A/H291A
458 displayed a rate of mitochondrial protein synthesis comparable to WT (Fig. 10d-g). Although
459 K245 and K295 stabilize the same beta phosphate on GDP, it is possible that H291 can
460 compensate for the loss of K295, explaining the decreased stability of the R177A/K245A mutant
461 compared to the R177A/K295A mutant. Change of nearby hydrophobic residues Y173A/Y208A
462 yields a decrease in translation similar to the R177A/K245A implying their role in GDP
463 stabilization (Fig. 10d-g). Lastly, double mutant pairs V209P/D238A and Y208A/D238A, which
464 directly disrupt GDP base binding to the mS29 β-hairpin, showed drastic decreases in the
465 synthesis and stability of mitochondrion-encoded proteins (Fig. 10d-g). Thus, the biochemical
466 assays based on mutagenesis show that GDP binding to mS29 is required for efficient
467 mitochondrial translation. Our structure-function correlation analyses suggest that GDP acts as a

stabilizing agent for mS29 β-hairpin 208-216 to maintain the intersubunit communication as tRNA moves to the hybrid state.

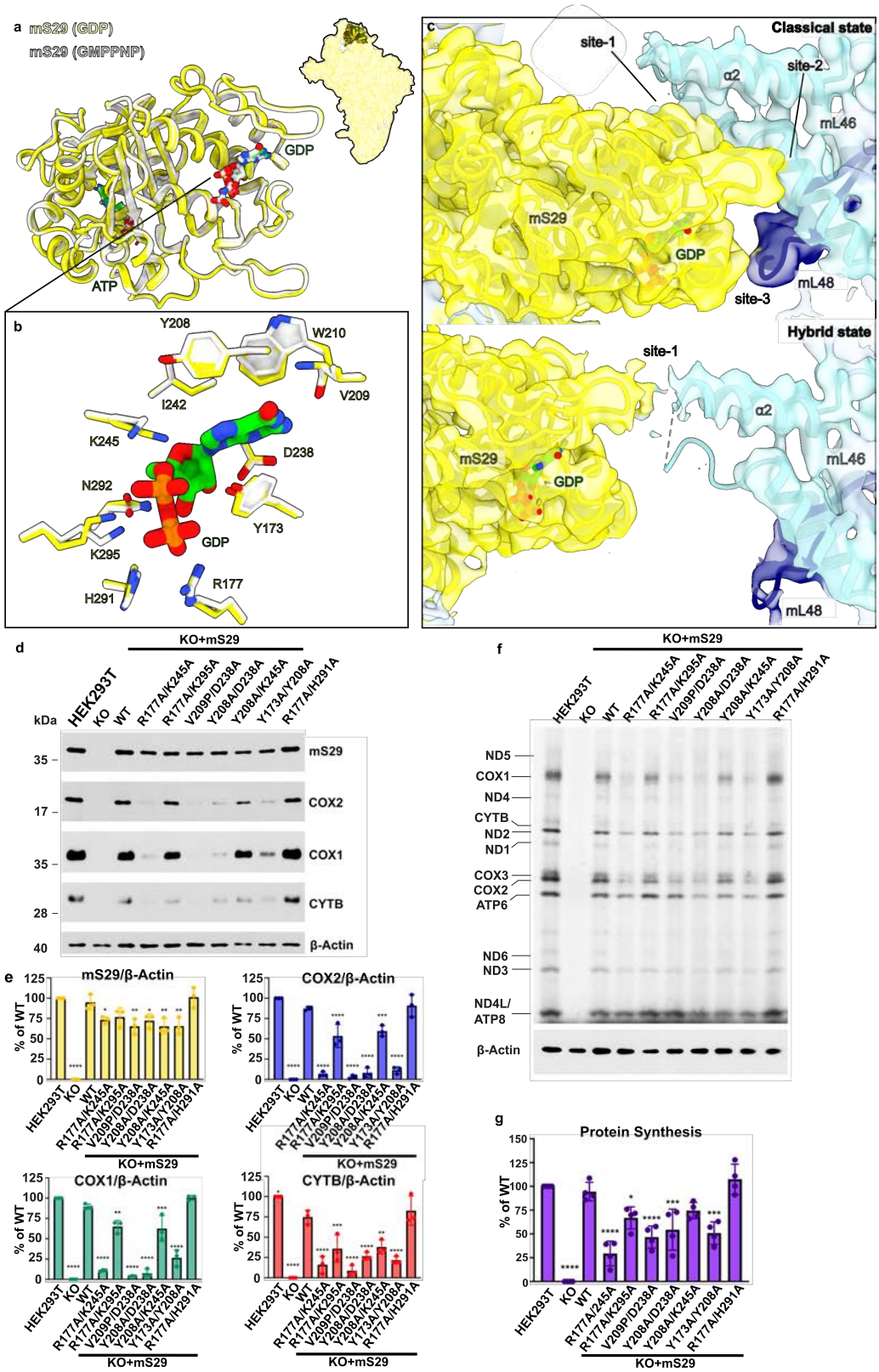

Fig. 10: Binding of GDP to mS29 and role in mitoribosome function.

472 **a,** Superposition of GDP-bound (yellow) and GMPPNP-bound (white) states. **b,** Close-up view
473 illustrating side chains that coordinate nucleotide binding. **c,** Intersubunit contacts in the classical
474 and hybrid states mediated by mS29 (cryo-EM density map shown as colored surface). **d**,
475 Immunoblot analysis comparing steady-state levels of proteins using whole cell lysates from
476 HEK293T (WT), *mS29*-KO (KO), and *mS29*-KO cells stably expressing either WT mS29 or
477 double mutants targeting the GDP-mS29β-hairpin binding site under the control of an attenuated
478 CMV6 promoter (Δ5pCMV6). COX1, COX2, and CTYB were used as markers of mitoribosome
479 function, and β-Actin was used as a loading control. **e**, Images in panel (d) were digitalized, and
480 densitometry was conducted using the histogram function in Adobe Photoshop. The bar graphs
481 represent the mean ± SD from three independent repetitions. Statistical differences were
482 estimated using one-way ANOVA in GraphPad Prism. *p<0.05, **p<0.01; ***p<0.001,
483 ****p<0.0001. **f**, Metabolic labeling of mitochondrially translated peptides in whole cells from
484 the indicated cell lines using ^{35}S-methionine for 15 minutes in the presence of emetine to inhibit
485 cytosolic protein synthesis. Immunoblotting for β-ACTIN was used as a loading control. Newly
486 synthesized peptides are identified on the left. **g**, Images in panel (d) were digitalized, and
487 densitometry was conducted using the histogram function in Adobe Photoshop. The bar graphs
488 represent the mean ± SD from four independent repetitions. Statistical differences were
489 estimated using one-way ANOVA in GraphPad Prism. *p<0.05, **p<0.01; ***p<0.001,
490 ****p<0.0001. The source data file contains all original uncropped and unprocessed
491 immunoblots as well as densitometry values used to perform statistics and generate
492 quantification graphs in panels (d-g).
493

494 **Discussion**

495 This study illustrates the modifications and cofactors of the human mitoribosome (Fig. 1-4,
496 Supplementary Fig. 3-5) and explains how mRNA and tRNAs are stabilized (Fig. 5-9,
497 Supplementary movie 1). While the basic mechanism of translation and the rRNA in the
498 decoding center are conserved, our structures attribute additional roles to mitoribosomal proteins
499 in mRNA and tRNA binding.

500 For mRNA, previous work showed that the delivery of some mitochondrial transcripts for
501 translation is facilitated by the factor LRPPRC [65, 66]. We now demonstrate that once an mRNA is
502 received by the mitoribosome, it involves six mitochondria-specific proteins that sequentially
503 help to direct the mRNA to the decoding center, where it's aligned with a tRNA (Fig. 5,6,
504 Supplementary Fig. 6,8-9). Most of these proteins compensate for the reduced rRNA through the
505 mechanisms of structural patching [67] and protein ratcheting [68] that drive neutral evolution of
506 protein complexity. The first protein to receive an mRNA is mS39, and we detected a co-
507 evolution of mS39 with an mRNA motif Y-N-C-Y that is enriched in all 12 transcripts encoded
508 in the heavy strand of the mitochondrial DNA. The only mRNA that is not enriched with the
509 motif is ND6 (Fig. 5, Supplementary Fig. 7). Interestingly, *ND6* possesses a long 3′UTR and is
510 the only transcript in human mitochondria lacking a polyA tail. This gene is also the only one in
511 mitochondria of vertebrates that was found to be translocated to the control region through gene

duplication [69]. This occurs in Antarctic fish species, and while the selectively advantageous duplicate is functionally neutral on the protein level [70], we found that there is a change in the Y-N-C-Y frequency in the mRNA sequence, which is increased by 2-fold (from 14 to 30 occurrences in 525 residues). It suggests a possible adaptive correlation between the mRNA stability on the mitoribosome and mt-DNA reorganization.

For tRNA, the structure demonstrates two cases with an involvement of mitoribosomal proteins. First, between the A- and P-site tRNAs, the N-terminus of mL40 extends from the CP to the phosphate backbone of mRNA. Second, the recognition of a tRNA in the E-site is achieved by a protein-made L1 stalk region and mL64. Both architectures are unique to mitochondria. Our molecular dynamics simulations further illustrate how the process of E-tRNA movement fundamentally relies on specific protein extensions and insertions of uL1m and uL9m without any involvement of rRNA (Fig. 8,9, Supplementary movie 2). These adaptations of mitoribosomal proteins are particularly important in the context of different functional states, as previous structural studies of elongation [8], termination [10], and rescue [6] complexes reported unidentified densities associated with translational factors, which we now assign specific proteins. Since our data resolves those densities as mammalian protein extensions (Fig. 5, Supplementary Fig. 6), the structural information can now be used for reinterpretation of the functional complexes, thus completing previous works.

In addition to proteins, newly revealed structural details include polyamines as stabilizing intramolecular agents in human mitochondria. The visualization of polyamines in the human mitoribosome and the reduced occupancy in the presence of antibiotics further supports their stimulating effect on mitochondrial translation, which is essential for cell proliferation. In mitoribosomes from cell culture treated with antibiotics [45, 71], the occupancy of the polyamines is reduced [45], and they are generally replaced with Mg^{2+}or K^{+}, accompanied by some residue rearrangement (Supplementary Fig. 5). Those changes are associated with attenuation of translation, and thus our structure rationalizes previous report that the positive effect of polyamines could not be functionally replaced by the addition of Mg^{2+} in a cell-free system [72]. Together, it links mitochondrial translation to reports assigning key regulatory effects to polyamines in mitochondria. This includes anti-inflammatory effects and inhibition of aging-associated pathologies upon consumption of polyamine in mice [31, 32, 73], the ability to boost mitochondrial respiratory capacity in a *Drosophila* aging model [32], restorative effects on oxidative functions of aged mitochondria [74, 75], and antitumor immunity in aged mice [76]. Polyamines were also proposed to regulate mitochondrial metabolism via Src kinase signaling to preserve bioenergetics in the spinal cord [77]. Considering our results on the involvement of iron-sulphur clusters as protein-protein mediating agents [45], as well as in the mitoribosomal assembly [78], the new structural data provides a wealth of additional information on cofactors that can be further assessed in disease models and with respect to tissue and cell specificity, as well as ageing processes. The detection of disulfide bond in mS37 that was proposed to occur during the mitochondrial protein import pathway [47] further links translation with metabolic state and

551 NADH/NAD$^+$ ratio in the intermembrane space and the matrix due to the special role of mS37
552 that links assembly to the initiation of translation [25].
553 On the rRNA level, through tailored quantitative mass-spectrometry, we describe a fully
554 modified mitoribosome, including in the decoding center. While the critical modifications are
555 conserved with bacteria, an unexpected feature of the structure is that the rRNA component CP-
556 tRNA^{Val} is modified, as well as aminoacylated. This suggests that this tRNA is recognized in the
557 matrix by the elongation factor mtEF-Tu prior the assembly onto the CP. The involvement
558 mtEF-Tu in the mitoribosome assembly has been previously reported, and direct interaction with
559 the assembly factor GTPBP5 was visualized by cryo-EM of an LSU intermediate [79]. Thus, the
560 regulation of the assembly of the mammalian mitoribosome relies on the availability of mtEF-Tu
561 in active developmental stages of the organelle, which might be a potential early checkpoint for
562 translation. A possible model for these observations is that accumulation of deacylated tRNAs
563 might trigger starvation responses, and since tRNA^{Val} is likely to be abundant at the onset of
564 mitoribosomal assembly, its aminoacylation is essential, which requires the presence of mtEF-
565 Tu. The feature is likely to be mammalian-specific, as representative from other lineages, such as
566 fungi [46], ciliates [80], and algae [81, 82] do not possess the CP-tRNA component in their
567 mitoribosomes.

568 Finally, the data addresses a long-standing question of whether a putative GTPase and death-
569 associated protein mS29 might provide the human mitoribosome with an intrinsic activity, while
570 undergoing structural rearrangements. This protein is of a particular clinical interest, because
571 several cancer types are associated with its aberrant expression [83]. We show that mS29-GDP
572 does not change its conformation during translation but is a stable structural element that
573 contributes to inter-subunit communication during transitions between classical and hybrid states
574 (Fig. 10, Supplementary Fig. 11).

575 Overall, these data explain how the newly identified components modulate the functional and
576 structurally distinct mitoribosome. With the continuous progress in improvement of resolution of
577 cryo-EM reconstructions, and availability of newly developed methods for base editing of
578 protein-coding genes in mammalian mitochondrial genome [84, 85], the field of mitochondrial
579 translation now steps into a phase, where it becomes possible to analyze fine regulatory
580 mechanisms specific transcripts, and study how it's affected by modifications, cofactors, and
581 mutants. Therefore, the structural approach has a potential to lead towards a more detailed
582 description of the mitoribosome-associated pathologies, including mitochondrial disease and
583 ageing, and the current study will provide a reference model of the human mitoribosome for
584 future investigation.

585

586 **References**

587 1. Kienzle L*, et al.* A small protein coded within the mitochondrial canonical gene nd4
588 regulates mitochondrial bioenergetics. *BMC Biol* **21**, 111 (2023).
589

590 2. Amunts A, Brown A, Toots J, Scheres SHW, Ramakrishnan V. Ribosome. The structure
591 of the human mitochondrial ribosome. *Science* **348**, 95-98 (2015).
592
593 3. Ferrari A, Del'Olio S, Barrientos A. The Diseased Mitoribosome. *FEBS Lett* **595**, 1025-
594 1061 (2021).
595
596 4. Amarasekera SSC*, et al.* Multi-omics identifies large mitoribosomal subunit instability
597 caused by pathogenic MRPL39 variants as a cause of pediatric onset mitochondrial
598 disease. *Hum Mol Genet*, (2023).
599
600 5. Aibara S, Singh V, Modelska A, Amunts A. Structural basis of mitochondrial translation.
601 *Elife* **9**, (2020).
602
603 6. Desai N, Yang H, Chandrasekaran V, Kazi R, Minczuk M, Ramakrishnan V.
604 Elongational stalling activates mitoribosome-associated quality control. *Science* **370**,
605 1105-1110 (2020).
606
607 7. Koripella RK*, et al.* Structures of the human mitochondrial ribosome bound to EF-G1
608 reveal distinct features of mitochondrial translation elongation. *Nat Commun* **11**, 3830
609 (2020).
610
611 8. Kummer E, Ban N. Structural insights into mammalian mitochondrial translation
612 elongation catalyzed by mtEFG1. *EMBO J* **39**, e104820 (2020).
613
614 9. Kummer E*, et al.* Unique features of mammalian mitochondrial translation initiation
615 revealed by cryo-EM. *Nature* **560**, 263-267 (2018).
616
617 10. Kummer E, Schubert KN, Schoenhut T, Scaiola A, Ban N. Structural basis of translation
618 termination, rescue, and recycling in mammalian mitochondria. *Mol Cell* **81**, 2566-2582
619 e2566 (2021).
620
621 11. Rebelo-Guiomar P, Powell CA, Van Haute L, Minczuk M. The mammalian
622 mitochondrial epitranscriptome. *Biochim Biophys Acta Gene Regul Mech* **1862**, 429-446
623 (2019).
624
625 12. D'Souza AR, Minczuk M. Mitochondrial transcription and translation: overview. *Essays*
626 *Biochem* **62**, 309-320 (2018).
627
628 13. Garone C*, et al.* Defective mitochondrial rRNA methyltransferase MRM2 causes
629 MELAS-like clinical syndrome. *Hum Mol Genet* **26**, 4257-4266 (2017).
630
631 14. Lopez Sanchez MIG, Cipullo M, Gopalakrishna S, Khawaja A, Rorbach J. Methylation
632 of Ribosomal RNA: A Mitochondrial Perspective. *Front Genet* **11**, 761 (2020).
633

15. Antonicka H, Choquet K, Lin ZY, Gingras AC, Kleinman CL, Shoubridge EA. A pseudouridine synthase module is essential for mitochondrial protein synthesis and cell viability. *EMBO Rep* **18**, 28-38 (2017).

16. Baer RJ, Dubin DT. Methylated regions of hamster mitochondrial ribosomal RNA: structural and functional correlates. *Nucleic Acids Res* **9**, 323-337 (1981).

17. McCulloch V, Seidel-Rogol BL, Shadel GS. A human mitochondrial transcription factor is related to RNA adenine methyltransferases and binds S-adenosylmethionine. *Mol Cell Biol* **22**, 1116-1125 (2002).

18. Metodiev MD*, et al.* Methylation of 12S rRNA is necessary for in vivo stability of the small subunit of the mammalian mitochondrial ribosome. *Cell Metab* **9**, 386-397 (2009).

19. Metodiev MD*, et al.* NSUN4 is a dual function mitochondrial protein required for both methylation of 12S rRNA and coordination of mitoribosomal assembly. *PLoS Genet* **10**, e1004110 (2014).

20. Seidel-Rogol BL, McCulloch V, Shadel GS. Human mitochondrial transcription factor B1 methylates ribosomal RNA at a conserved stem-loop. *Nat Genet* **33**, 23-24 (2003).

21. Sergiev PV, Aleksashin NA, Chugunova AA, Polikanov YS, Dontsova OA. Structural and evolutionary insights into ribosomal RNA methylation. *Nat Chem Biol* **14**, 226-235 (2018).

22. Van Haute L*, et al.* METTL15 introduces N4-methylcytidine into human mitochondrial 12S rRNA and is required for mitoribosome biogenesis. *Nucleic Acids Res* **47**, 10267-10281 (2019).

23. Zaganelli S*, et al.* The Pseudouridine Synthase RPUSD4 Is an Essential Component of Mitochondrial RNA Granules. *J Biol Chem* **292**, 4519-4532 (2017).

24. Hillen HS*, et al.* Structural basis of GTPase-mediated mitochondrial ribosome biogenesis and recycling. *Nat Commun* **12**, 3672 (2021).

25. Itoh Y*, et al.* Mechanism of mitoribosomal small subunit biogenesis and preinitiation. *Nature* **606**, 603-608 (2022).

26. Harper NJ, Burnside C, Klinge S. Principles of mitoribosomal small subunit assembly in eukaryotes. *Nature* **614**, 175-181 (2023).

27. Bobba-Alves N*, et al.*, (2022).

28. Haas RH. Mitochondrial Dysfunction in Aging and Diseases of Aging. *Biology (Basel)* **8**, (2019).

680 29. Hong HJ, *et al.* Mitoribosome insufficiency in beta cells is associated with type 2
681 diabetes-like islet failure. *Exp Mol Med* **54**, 932-945 (2022).
682
683 30. Richman TR, *et al.* Mitochondrial mistranslation modulated by metabolic stress causes
684 cardiovascular disease and reduced lifespan. *Aging Cell* **20**, e13408 (2021).
685
686 31. Soda K, Dobashi Y, Kano Y, Tsujinaka S, Konishi F. Polyamine-rich food decreases age-
687 associated pathology and mortality in aged mice. *Exp Gerontol* **44**, 727-732 (2009).
688
689 32. Soda K, Kano Y, Chiba F, Koizumi K, Miyaki Y. Increased polyamine intake inhibits
690 age-associated alteration in global DNA methylation and 1,2-dimethylhydrazine-induced
691 tumorigenesis. *PLoS One* **8**, e64357 (2013).
692
693 33. Medina CB, *et al.* Metabolites released from apoptotic cells act as tissue messengers.
694 *Nature* **580**, 130-135 (2020).
695
696 34. Igarashi K, Kashiwagi K. The functional role of polyamines in eukaryotic cells. *Int J*
697 *Biochem Cell Biol* **107**, 104-115 (2019).
698
699 35. Mandal S, Mandal A, Johansson HE, Orjalo AV, Park MH. Depletion of cellular
700 polyamines, spermidine and spermine, causes a total arrest in translation and growth in
701 mammalian cells. *Proc Natl Acad Sci U S A* **110**, 2169-2174 (2013).
702
703 36. Zivanov J, *et al.* New tools for automated high-resolution cryo-EM structure
704 determination in RELION-3. *Elife* **7**, (2018).
705
706 37. Zivanov J, Nakane T, Scheres SHW. A Bayesian approach to beam-induced motion
707 correction in cryo-EM single-particle analysis. *IUCrJ* **6**, 5-17 (2019).
708
709 38. Zivanov J, Nakane T, Scheres SHW. Estimation of high-order aberrations and anisotropic
710 magnification from cryo-EM data sets in RELION-3.1. *IUCrJ* **7**, 253-267 (2020).
711
712 39. Scheres SH. Processing of Structurally Heterogeneous Cryo-EM Data in RELION.
713 *Methods Enzymol* **579**, 125-157 (2016).
714
715 40. Taoka M, *et al.* A mass spectrometry-based method for comprehensive quantitative
716 determination of post-transcriptional RNA modifications: the complete chemical
717 structure of Schizosaccharomyces pombe ribosomal RNAs. *Nucleic Acids Res* **43**, e115
718 (2015).
719
720 41. Brown A, *et al.* Structure of the large ribosomal subunit from human mitochondria.
721 *Science* **346**, 718-722 (2014).
722
723 42. Brown A, *et al.* Structures of the human mitochondrial ribosome in native states of
724 assembly. *Nat Struct Mol Biol* **24**, 866-869 (2017).
725

43. Greber BJ, *et al.* The complete structure of the large subunit of the mammalian mitochondrial ribosome. *Nature* **515**, 283-286 (2014).

44. Suzuki T, *et al.* Complete chemical structures of human mitochondrial tRNAs. *Nat Commun* **11**, 4269 (2020).

45. Itoh Y, *et al.* Structure of the mitoribosomal small subunit with streptomycin reveals Fe-S clusters and physiological molecules. *Elife* **11**, (2022).

46. Itoh Y, Naschberger A, Mortezaei N, Herrmann JM, Amunts A. Analysis of translating mitoribosome reveals functional characteristics of translation in mitochondria of fungi. *Nat Commun* **11**, 5187 (2020).

47. Peker E, *et al.* A two-step mitochondrial import pathway couples the disulfide relay with matrix complex I biogenesis. *J Cell Biol* **222**, (2023).

48. Watson ZL, *et al.* Structure of the bacterial ribosome at 2 A resolution. *Elife* **9**, (2020).

49. Jourdain AA, *et al.* A mitochondria-specific isoform of FASTK is present in mitochondrial RNA granules and regulates gene expression and function. *Cell Rep* **10**, 1110-1121 (2015).

50. Takyar S, Hickerson RP, Noller HF. mRNA helicase activity of the ribosome. *Cell* **120**, 49-58 (2005).

51. Khawaja A, *et al.* Distinct pre-initiation steps in human mitochondrial translation. *Nat Commun* **11**, 2932 (2020).

52. Selmer M, *et al.* Structure of the 70S ribosome complexed with mRNA and tRNA. *Science* **313**, 1935-1942 (2006).

53. Rozov A, *et al.* Importance of potassium ions for ribosome structure and function revealed by long-wavelength X-ray diffraction. *Nat Commun* **10**, 2519 (2019).

54. Bhaskar V, *et al.* Dynamics of uS19 C-Terminal Tail during the Translation Elongation Cycle in Human Ribosomes. *Cell Rep* **31**, 107473 (2020).

55. Ogle JM, Brodersen DE, Clemons WM, Jr., Tarry MJ, Carter AP, Ramakrishnan V. Recognition of cognate transfer RNA by the 30S ribosomal subunit. *Science* **292**, 897-902 (2001).

56. Youngman EM, Cochella L, Brunelle JL, He S, Green R. Two distinct conformations of the conserved RNA-rich decoding center of the small ribosomal subunit are recognized by tRNAs and release factors. *Cold Spring Harb Symp Quant Biol* **71**, 545-549 (2006).

57. Nakayama H, *et al.* Ariadne: a database search engine for identification and chemical analysis of RNA using tandem mass spectrometry data. *Nucleic Acids Res* **37**, e47 (2009).

58. Yamauchi Y, *et al.* A mass spectrometry-based method for direct determination of pseudouridine in RNA. *Nucleic Acids Res* **44**, e59 (2016).

59. Nishimura K, *et al.* Identification of the RsmG methyltransferase target as 16S rRNA nucleotide G527 and characterization of Bacillus subtilis rsmG mutants. *J Bacteriol* **189**, 6068-6073 (2007).

60. Noel JK, *et al.* SMOG 2: A Versatile Software Package for Generating Structure-Based Models. *PLoS Comput Biol* **12**, e1004794 (2016).

61. Whitford PC, Noel JK, Gosavi S, Schug A, Sanbonmatsu KY, Onuchic JN. An all-atom structure-based potential for proteins: bridging minimal models with all-atom empirical forcefields. *Proteins* **75**, 430-441 (2009).

62. Polikanov YS, Melnikov SV, Soll D, Steitz TA. Structural insights into the role of rRNA modifications in protein synthesis and ribosome assembly. *Nat Struct Mol Biol* **22**, 342-344 (2015).

63. Greber BJ, *et al.* Ribosome. The complete structure of the 55S mammalian mitochondrial ribosome. *Science* **348**, 303-308 (2015).

64. Ott M, Amunts A, Brown A. Organization and Regulation of Mitochondrial Protein Synthesis. *Annu Rev Biochem* **85**, 77-101 (2016).

65. Singh V, *et al.* Structural basis of LRPPRC-SLIRP-dependent translation by the mitoribosome. *bioRxiv*, 2022.2006.2020.496763 (2022).

66. Webster MW, *et al.* Structural basis of transcription-translation coupling and collision in bacteria. *Science* **369**, 1355-1359 (2020).

67. Petrov AS, Wood EC, Bernier CR, Norris AM, Brown A, Amunts A. Structural Patching Fosters Divergence of Mitochondrial Ribosomes. *Mol Biol Evol* **36**, 207-219 (2019).

68. Hochberg GKA, Liu Y, Marklund EG, Metzger BPH, Laganowsky A, Thornton JW. A hydrophobic ratchet entrenches molecular complexes. *Nature* **588**, 503-508 (2020).

69. Zhuang X, Cheng CH. ND6 gene "lost" and found: evolution of mitochondrial gene rearrangement in Antarctic notothenioids. *Mol Biol Evol* **27**, 1391-1403 (2010).

70. Mark FC, *et al.* Mitochondrial function in Antarctic nototheniids with ND6 translocation. *PLoS One* **7**, e31860 (2012).

71. Itoh Y, *et al.* Mechanism of membrane-tethered mitochondrial protein synthesis. *Science* **371**, 846-849 (2021).

72. Ogasawara T, Ito K, Igarashi K. Effect of polyamines on globin synthesis in a rabbit reticulocyte polyamine-free protein synthetic system. *J Biochem* **105**, 164-167 (1989).

73. Schroeder S, *et al.* Dietary spermidine improves cognitive function. *Cell Rep* **35**, 108985 (2021).

74. Jing YH, *et al.* Spermidine ameliorates the neuronal aging by improving the mitochondrial function in vitro. *Exp Gerontol* **108**, 77-86 (2018).

75. Phillips JE, Chaffee RR. Restorative effects of spermine on oxidative phosphorylation and respiration in heat-aged mitochondria. *Biochem Biophys Res Commun* **108**, 174-181 (1982).

76. Al-Habsi M, *et al.* Spermidine activates mitochondrial trifunctional protein and improves antitumor immunity in mice. *Science* **378**, eabj3510 (2022).

77. Zhang R, Ma XN, Liu K, Zhang L, Yao M. Exogenous spermine preserves mitochondrial bioenergetics via regulating Src kinase signaling in the spinal cord. *Mol Med Rep* **16**, 3619-3626 (2017).

78. Ast T, *et al.* METTL17 is an Fe-S cluster checkpoint for mitochondrial translation. *bioRxiv*, 2022.2011.2024.517765 (2022).

79. Cipullo M, Gese GV, Khawaja A, Hallberg BM, Rorbach J. Structural basis for late maturation steps of the human mitoribosomal large subunit. *Nat Commun* **12**, 3673 (2021).

80. Tobiasson V, Amunts A. Ciliate mitoribosome illuminates evolutionary steps of mitochondrial translation. *Elife* **9**, (2020).

81. Tobiasson V, Gahura O, Aibara S, Baradaran R, Zikova A, Amunts A. Interconnected assembly factors regulate the biogenesis of mitoribosomal large subunit. *EMBO J* **40**, e106292 (2021).

82. Waltz F, Soufari H, Bochler A, Giege P, Hashem Y. Cryo-EM structure of the RNA-rich plant mitochondrial ribosome. *Nat Plants* **6**, 377-383 (2020).

83. Sui L, *et al.* Death associated protein-3 (DAP3) and DAP3 binding cell death enhancer-1 (DELE1) in human colorectal cancer, and their impacts on clinical outcome and chemoresistance. *Int J Oncol* **62**, (2023).

84. Silva-Pinheiro P, *et al.* A library of base editors for the precise ablation of all protein-coding genes in the mouse mitochondrial genome. *Nat Biomed Eng*, (2022).

85. Willis JCW, Silva-Pinheiro P, Widdup L, Minczuk M, Liu DR. Compact zinc finger base editors that edit mitochondrial or nuclear DNA in vitro and in vivo. *Nat Commun* **13**, 7204 (2022).

Methods

Experimental model and culturing

HEK293S-derived cells (T501) were grown in Freestyle 293 Expression Medium containing 5% tetracycline-free fetal bovine serum (FBS) in vented shaking flasks at 37°C, 5% CO_2 and 120 rpm (550 x g). Culture was scaled up sequentially, by inoculating at 1.5 x 10^6 cells/mL and subsequently splitting at a cell density of 3.0 x 10^6 cells/mL. Finally, a final volume of 2 L of cell culture at a cell density of 4.5 x 10^6 cells/mL was used for mitochondria isolation, as previously described [86].

mS29-KO cells were derived from HEK293T (CRL-3216) and cultured in complete DMEM supplemented with 20% FBS at 37 °C and 5% CO_2. HEK293T (CRL-3216) were cultured in high-glucose, sodium pyruvate, L-glutamine Dulbecco's modified Eagle medium (DMEM, Life Technologies) supplemented with 10% FBS, 100 µg/mL uridine, 3 mM sodium formate, and 1x MEM non-essential amino acids complete DMEM medium). Analysis of mycoplasma contamination was routinely performed.

For the labeling of cells with deuterated Uridine required for SILNAS analysis, TK6 cells deficient in uridine monophosphate synthase (*UMPS-/-*) were cultured at 37°C in RPMI-1640 medium containing 10% horse serum, 2 mM L-glutamine, penicillin (50 U/ml), streptomycin (50 µg/ml) and 0.1 mM 5,6-D2-uridine.

Generation of mS29 edited cell lines and plasmid transfections

To generate a stable human *mS29-KO* cell line in HEK293T cells (ATCC: CRL-3216), we used a pool of CRISPR/Cas9-mediated knockout cells generated by the genome editing company, Synthego (Synthego Corporation, Redwood City, CA). HEK293T cells were first tested to be negative for mycoplasma. Three guide RNAs targeting exon 5 of the *mS29* gene (DAP3-202 transcript ID ENST00000368336.10) were selected for high specificity and activity to create premature stop codons through frameshift mutations in the coding region via insertions and/or deletions (Indels). Targeting exon 5 ensured that all *mS29* transcript variants would be affected. Based on additional off-target analysis, the three specific guide RNAs selected (g1, g2, and g3) were: g1 5′-GUGAAGCUUGCCUGAUGGUA-3′ [AGG]-PAM, g2 5′-UAUAGCUGGAUAAGCAAAAC-3′ [TGG]-PAM, and g3 5′-AUGCUUUCUCCCCUCAAAUA-3′ [AGG]-PAM. The pool of knockout cells was then generated by electroporation of ribonucleoproteins (RNPs) containing the Cas9 protein and synthetic chemically modified sgRNA (Synthego) into the cells using Synthego's optimized protocol. The editing efficiency was assessed upon recovery, 48 h post-electroporation. Genomic

901 DNA is extracted from a portion of the cells, PCR-amplified, and sequenced using Sanger
902 sequencing. The resulting chromatograms are processed using Synthego Inference of CRISPR
903 Edits software (ice.synthego.com). The pooled *mS29-KO* was then plated into 96-well plates to
904 screen for single clones in-house. Single clone candidates were screened by immunoblotting to
905 determine the steady-state levels of mS29 and the mtDNA-encoded COX2 protein as a surrogate
906 of mitochondrial protein synthesis capacity. Clones that had undetectable mS29 and attenuated
907 COX2 levels were further analyzed by genotyping. For genotyping, the edited region of mS29
908 was amplified using oligonucleotides mS29 exon 5 seq (-164) Forward: 5′-
909 GGATAGATTTTCAAACTCAGTACCA-3′ and mS29 exon 5 seq (+166) Reverse: 5′-
910 TCCTGACTTCAGGCGATACG-3′, and subsequently cloned into the TOPO-TA vector
911 (Thermo Fisher) for sequencing.

912 To establish a stable cell line reconstituted with mS29, we obtained the WT *mS29* gene as a
913 Myc/DDK-tagged ORF from Origene (Cat# RC223182). Using restriction sites *Asi*SI and *Pme*I,
914 WT mS29-Myc/DDK was cloned into a mammalian vector with hygromycin as the selection
915 marker. The vector used was pCMV6, in which mS29 gene expression was placed under the
916 control of an attenuated version of the human cytomegalovirus (CMV) enhancer/promoter (Δ5)
917 in which a deletion in the promoter sequence eliminates most transcription factor binding sites [87].
918 Furthermore, to ensure functionality of the recombinant mS29, the Myc/DDK tag was removed
919 via the Q5 site-directed mutagenesis kit (New England Biolabs) using the oligonucleotides mS29
920 ΔMyc-DDK Forward: 5′-TAAACGGCCGGCCGCGGT-3′ and mS29 Δmyc-DDK Reverse: 5′-
921 GAGGTAGGCACAGTGCCGCTC-3′. Two µg of the construct containing *mS29* was
922 transfected to the HEK293T *mS29*-KO cell line using 5 µL of EndoFectin™ Max (GeneCopoeia)
923 pre-incubated in Opti-MEM (ThermoFisher). 72 h post-transfection, the medium was
924 supplemented with 200µg/mL hygromycin B for three weeks. We use the same protocol to
925 establish stable cell lines reconstituted with mutant variants of mS29.

926 Mutant variants of the *mS29*-containing construct were generated using the Q5 site-directed
927 mutagenesis kit (New England Biolabs). Mutagenesis primers were designed using the
928 NEBaseChanger tool. Oligonucleotides used for mutagenesis include: mS29 K134A Forward:
929 5′-GGGAACAGGAGCAACCCTAAGTC-3′; mS29 K134A Reverse: 5′-
930 TTCTCTCCATACAGAAGATATC-3′; mS29 Y173A Forward: 5′-
931 GCAGTCCAGCGCCAACAAACAGC-3′; mS29 Y173A Reverse: 5′-
932 AGAAGATCCCGACAATTTTTC-3′; mS29 R177A Forward: 5′-
933 CAACAAACAGGCCTTTGATCAACCTTTAGAG-3′; mS29 R177A Reverse: 5′-
934 TAGCTGGACTGCAGAAGA-3′; mS29 K245A Forward: 5′-
935 AATTGTGCTGGCAGAGCTAAAGAGGC-3′; mS29 K245A Reverse: 5′-
936 CCAACTGCATCTGTGGCG-3′; mS29 H291A Forward: 5′-
937 AGCACTTGTTGCCAACTTGAGGAAAATGATG-3′; mS29 H291A Reverse: 5′-
938 AATTCCTCGGGGGCAATC-3′; mS29 K295A Forward: 5′-
939 CAACTTGAGGGCAATGATGAAAAATGATTG-3′; mS29 K295A Reverse: 5′-
940 TGAACAAGTGCTAATTCC-3′; mS29 Y208A Forward: 5’-

941 TCAAGAGAAGGCTGTCTGGAATAAGAG -3'; mS29 Y208A Reverse: 5'-
942 ACTTTTATCTGGTTCAGG -3'; mS29 V209P Forward: 5'-
943 AGAGAAGTATCCCTGGAATAAGAGAG -3'; mS29 V209P Reverse: 5'-
944 TGAACTTTTATCTGGTTCAG -3'; mS29 D238A Forward: 5'-
945 GAACGCCACAGCTGCAGTTGGAA -3'; mS29 D238A Reverse: 5'-
946 CTCACCCGTGTTATGCCC -3. All mutant sequences were validated by Sanger sequencing
947 using oligonucleotides Δ5pCMV6 Forward: 5′-CCTCTTCGCTATTACGCCAG-3′, mS29
948 cDNA (308) Forward: 5′-AACCAGCCCTAGAACTTCTGC-3′, and mS29 cDNA (829)
949 Forward: 5′-GAAGATAAAAGCCCGATTGC-3′.
950

951 Mitoribosome purification

952 Mitoribosome purification was carried out based on the previously developed protocol for rapid
953 isolation [86]. HEK293S-derived cells were harvested from the 2 L culture when the cell density
954 was 4.2 x 10^6 cells/mL by centrifugation at 1,000 g for 7 min, 4 °C. The pellet was washed and
955 resuspended in 200 mL Phosphate Buffered Saline (PBS). The washed cells were pelleted at
956 1,000 g for 10 min at 4 °C. The resulting pellet was resuspended in 120 mL of MIB buffer (50
957 mM HEPES-KOH, pH 7.5, 10 mM KCl, 1.5 mM $MgCl_2$, 1 mM EDTA, 1 mM EGTA, 1 mM
958 dithiothreitol, cOmplete EDTA-free protease inhibitor cocktail (Roche) and allowed to swell in
959 the buffer for 15 min in the cold room by gentle stirring. About 45 mL of SM4 buffer (840 mM
960 mannitol, 280 mM sucrose, 50 mM HEPES-KOH, pH 7.5, 10 mM KCl, 1.5 mM $MgCl_2$, 1 mM
961 EDTA, 1 mM EGTA, 1 mM DTT, 1X cOmplete EDTA-free protease inhibitor cocktail (Roche)
962 was added to the cells in being stirred in MIB buffer and poured into a nitrogen cavitation device
963 kept on ice. The cells were subjected to a pressure of 500 psi for 20 min before releasing the
964 nitrogen from the chamber and collecting the lysate. The lysate was clarified by centrifugation at
965 800 x g and 4 °C, for 15 min, to separate the cell debris and nuclei. The supernatant was passed
966 through a cheesecloth into a beaker kept on ice. The pellet was resuspended in half the previous
967 volume of MIBSM buffer (3 volumes MIB buffer + 1 volume SM4 buffer) and homogenized
968 with a Teflon/glass Dounce homogenizer. After clarification as described before, the resulting
969 lysate was pooled with the previous batch of the lysate and subjected to centrifugation at 1,000 x
970 g, 4 °C for 15 minutes to ensure complete removal of cell debris. The clarified and filtered
971 supernatant was centrifuged at 10,000 x g and 4 °C for 15 min to pellet crude mitochondria.
972 Crude mitochondria were resuspended in 10 mL MIBSM buffer and treated with 200 units of
973 Rnase-free Dnase (Sigma-Aldrich) for 20 min in the cold room to remove contaminating
974 genomic DNA. Crude mitochondria were again recovered by centrifugation at 10,000 g, 4 °C for
975 15 min and gently resuspended in 2 mL SEM buffer (250 mM sucrose, 20 mM HEPES-KOH,
976 pH 7.5, 1 mM EDTA). Resuspended mitochondria were subjected to a sucrose density step-
977 gradient (1.5 mL of 60% sucrose; 4 mL of 32% sucrose; 1.5 mL of 23% sucrose and 1.5 mL of
978 15% sucrose in 20 mM HEPES-KOH, pH 7.5, 1 mM EDTA) centrifugation in a Beckmann
979 Coulter SW40 rotor at 28,000 rpm (139,000 x g) for 60 min. Mitochondria seen as a brown band

980 at the interface of 32% and 60% sucrose layers were collected and snap-frozen using liquid
981 nitrogen and transferred to −80 °C.

982 Frozen mitochondria were transferred on ice and allowed to thaw slowly. Lysis buffer (25 mM
983 HEPES-KOH, pH 7.5, 50 mM KCl, 10 mM $Mg(OAc)_2$, 2% polyethylene glycol octylphenyl
984 ether, 2 mM DTT, 1 mg/mL EDTA-free protease inhibitors (Sigma-Aldrich) was added to
985 mitochondria and the tube was inverted several times to ensure mixing. A small Teflon/glass
986 Dounce homogenizer was used to homogenize mitochondria for efficient lysis. After incubation
987 on ice for 5-10 min, the lysate was clarified by centrifugation at 30,000 x g for 20 min, 4 °C. The
988 clarified lysate was carefully collected. Centrifugation was repeated to ensure complete
989 clarification. A volume of 1 mL of the mitochondrial lysate was applied on top of 0.4 mL of 1 M
990 sucrose (v/v ratio of 2.5:1) in thick-walled TLS55 tubes. Centrifugation was carried out at
991 231,500 x g for 45 min in a TLA120.2 rotor at 4 °C. The pellets thus obtained were washed and
992 sequentially resuspended in a total volume of 100 µl resuspension buffer (20 mM HEPES-KOH,
993 pH 7.5, 50 mM KCl, 10 mM $Mg(OAc)_2$, 1% Triton X-100, 2 mM DTT). The sample was
994 clarified twice by centrifugation at 18,000 g for 10 min at 4 °C. The sample was applied on to a
995 linear 15-30% sucrose (20 mM HEPES-KOH, pH 7.5, 50 mM KCl, 10 mM $Mg(OAc)_2$, 0.05% n-
996 dodecyl-β-D-maltopyranoside, 2 mM DTT) gradient and centrifuged in a TLS55 rotor at 213,600
997 x g for 120 min at 4 °C. The gradient was fractionated into 50 µL volume aliquots. The
998 absorption for each aliquot at 260 nm was measured and fractions corresponding to the
999 monosome peak were collected. The pooled fractions were subjected to buffer exchange with the
1000 resuspension buffer to dilute away sucrose.

1001

1002 <u>rRNA mass spectrometry</u>

1003 *Purification of mitochondrial rRNAs*

1004 Mitochondrial rRNAs of the HEK293 cells were extracted from the purified ribosome using
1005 Isogen (Nippon Gene) and stored at -80 °C until use. TK6 cell culture (~1.0×10^9 cells) were
1006 homogenized by Dounce homogenizer with 250 mM sucrose, 1 mM EDTA and 10 mM
1007 Tris−HCl (pH 8.0). The lysate was centrifuged twice at 1500 x g for 3 min at 4 °C, and the
1008 resulting supernatant was further centrifuged at 5000 x g for 10 min to obtain mitochondrial
1009 precipitate. From the precipitate, total mitochondrial RNA (~100 µg) was extracted using TRIzol
1010 Reagent (Thermo Fisher Scientific).

1011 Each mitochondrial rRNA was purified by using reversed-phase LC through a PLRP-S 4000Å
1012 column (4.6 × 150 mm, 10 µm, Agilent Technologies). After applying the mixture of rRNAs
1013 from the purified ribosome or total mitochondrial RNA to the column, the rRNAs were eluted
1014 with a 60-minute linear gradient of 11.5–13.5% (v/v) acetonitrile in 100 mM TEAA (pH 7.0) and
1015 0.1 mM diammonium phosphate at a flow rate of 200 µl/min at 60 °C while monitoring the
1016 eluate at A260 [88].

1017

1018 *LC-MS, MS/MS and MS/MS/MS analysis and database search of RNA fragments*

1019 RNA was digested as described below. Nucleolytic RNA fragments were analyzed with a direct
1020 nanoflow LC-MS system as described [89]. The LC eluate was sprayed online at –1.3 kV with the
1021 aid of a spray-assisting device [89] to a Q Exactive Plus mass spectrometer (Thermo Fisher
1022 Scientific) in negative ion mode. Other settings for MS, MS/MS and MS/MS/MS were as
1023 described [58].

1024 Ariadne [57] was used for database searches and assignment of MS/MS RNA spectra. The
1025 composite of human cytosolic and mitochondrial rRNA and tRNA sequences was used as a
1026 database. The following default search parameters for Ariadne were used: maximum number of
1027 missed cleavages, 1; variable modification parameters, two methylations per RNA fragment for
1028 any residue; RNA mass tolerance, ±5 ppm, and MS/MS tolerance, ±20 ppm. For assignment of
1029 Ψ residues using 5,6-D2-uridine labeled RNAs, the mass table and the variable modification
1030 parameters were altered from default values to "5,6D_CU" and "Ψ", respectively, because both
1031 C and U were labeled with the medium and the pseudouridylation reaction results in the
1032 exchange of the position 5 deuterium of 5,6-D2-uridine to the proton of solvent, providing a −1
1033 Da mass shift [52].

1034

1035 *Internal standard RNAs and SILNAS-based quantitation of the stoichiometry of post-*
1036 *transcriptional modification*

1037 To construct the plasmids for i*n vitro* transcription of internal standard RNAs, DNAs encoding
1038 human 12S and 16S rRNAs were amplified by PCR from the mitochondrial DNA from TK6
1039 cells. The PCR primers used are as follows: HindIII-12S-Forward
1040 TATAAAGCTTAATAGGTTTGGTCCTAGCCTTTCTATTAGC, 12S-*Bam*HI-reverse
1041 ATATGGATCCGTTCGTCCAAGTGCACTTTCCAGTACACTT, *Hind*III-16S-forward
1042 TATAAAGCTTGCTAAACCTAGCCCCAAACCCACTCCACCT and 16S-*Xho*I-reverse
1043 ATATCTCGAGAAACCCTGTTCTTGGGTGGGTGTGGGTATA). The amplified DNAs were
1044 inserted into the multiple cloning sites of plasmid pCDNA3.1 (+) (Thermo Fisher Scientific). To
1045 synthesize RNA, 2 μg of template DNA was incubated and transcribed using Megascript T7 kit
1046 (Thermo Fisher Scientific). When RNA was synthesized, guanosine-$^{13}C_{10}$ 5′-triphosphate,
1047 cytidine-$^{13}C_9$ 5′-triphosphate, or uridine-$^{13}C_9$ 5′-triphosphate solution was used instead of the
1048 respective 5′-triphosphate reagent that contained carbons with a natural isotope distribution. The
1049 RNA was precipitated in ethanol, solubilized in nuclease-free water, and purified further by
1050 reversed-phase LC as described above.

1051 SILNAS-based quantitation was performed as described [90]. In brief, RNA (~100 fmol) from
1052 natural sources or cells grown in guanosine with natural isotope distribution was mixed with an
1053 equal amount of synthetic RNA transcribed *in vitro* with ^{13}C-labeled guanosine and digested
1054 with RNAse T1 (2 ng/μl). For the RNA transcribed with $^{13}C_9$-labeled cytidine and uridine, Rnase
1055 A (0.5 ng/μl) was used as the digestion enzyme. Digestion was carried out in 100 mM TEAA
1056 (pH 7.0) at 37°C. The 1:1 RNA mixing was performed based on the measurement of the

1057 absorbance at 260 nm and ensured later by a correction factor obtained experimentally. After
1058 obtaining the LC-MS spectrum of the digested RNA mixture, the stoichiometry of RNA
1059 modification at each site was estimated by Ariadne program designed for SILNAS [90]. The results
1060 were confirmed by manual inspection of the original MS spectrum to examine whether the
1061 estimates are based on 'uncontaminated' MS signals.

1062

1063 *Other procedures for RNA analysis*

1064 The masses of RNA fragments and a-, c-, w-, and y-series ions were calculated with Ariadne
1065 (http://ariadne.riken.jp/). Sequence-specific Rnase H cleavage of rRNAs was performed as
1066 described [91], using O-methylated RNA/DNA hybrid oligonucleotide complementary to the 12S
1067 and 16S rRNAs,
1068 GmUmUmCmGmUmCm(CAAG)UmGmCmAmCmUmUmUmCmCmAmGmUmAmCmAmC
1069 m and (AmAmCmCmCmUmGm(TTCT)UmGmGmGmUmGmGmGmUm, respectively (where
1070 Nm refers to 2'-O-methyl ribonucleotide and deoxyribonucleotides are indicated in parentheses).

1071

1072 <u>SDS-PAGE and immunoblotting analyses</u>

1073 Whole-cell protein extracts were obtained by solubilization in RIPA buffer (25mM Tris-HCl pH
1074 7.6, 150 mM NaCl, 1% NP-40, 1% sodium deoxycholate, and 0.1% SDS) with 1 mM PMSF and
1075 1x mammalian protease inhibitor. Extracts were cleared by 5 minutes of centrifugation at 10,000
1076 g at 4 °C. Protein concentrations were determined with the Folin phenol reagent. 40-60 µg of
1077 whole-cell protein extracts were separated by SDS-PAGE in the Laemmli buffer system.
1078 Proteins were then transferred to nitrocellulose membranes, subsequently blocked with 5% skim
1079 milk, and then incubated with antibodies against the indicated proteins followed by a second
1080 reaction with anti-mouse or anti-rabbit IgG conjugated to horseradish peroxidase. Signals were
1081 detected by chemiluminescence and exposure to X-ray films. For quantification, the signals in
1082 digitalized images were quantified by densitometry using the histogram function of Adobe
1083 Photoshop. Values were normalized to the signal of β-Actin and plotted as the percentage of WT
1084 using the Prism 8 software.

1085

1086 <u>Pulse labeling of mitochondrial translation products</u>

1087 Mitochondrial protein synthesis was determined by pulse-labeling of 60-70% confluent human
1088 wild-type (WT) HEK293T cells, *MRPS29*-KO HEK293T cells, and knockout cells stably
1089 reconstituted with mutant *MRPS29* variants. Cultures were grown in a medium without
1090 methionine and in the presence of 100 µg/mL emetine to inhibit cytoplasmic translation as
1091 described [92, 93]. Cells were labeled for 15 min at 37 °C with 100 µCi of ^{35}S-methionine
1092 (PerkinElmer Life Sciences, Boston, MA). After incubation, the medium containing ^{35}S-
1093 methionine was removed, the cells were washed once with PBS, and then the cells were
1094 incubated for 5 minutes in complete DMEM to allow recovery. After the short incubation, cells

1095 were washed once more with PBS, collected by trypsinization, and whole-cell protein extracts
1096 were obtained by solubilization with RIPA buffer. 40-50 µg of each sample was separated by
1097 SDS-PAGE on a 17.5% polyacrylamide gel, transferred to a nitrocellulose membrane, and
1098 exposed to X-ray film. Membranes were then probed by immunoblotting to assess the steady-
1099 state levels of β-ACTIN as a loading control. Values were normalized to the signal of β-ACTIN
1100 and plotted as the percentage of WT using the Prism 8 software. Potassium cyanide (KCN)-
1101 sensitive endogenous cell respiration was measured polarographically using a Clark electrode in
1102 the indicated cell lines. Cell respiration rates are presented as nmol of O_2 consumed per one
1103 million cells per minute.

1104

1105 Cryo-EM data acquisition

1106 Five cryo-EM datasets of mitoribosomal complexes were collected in total using EPU 1.9
1107 (Extended Data Table 1). First, 3 µL of ~120 nM mitoribosome was applied onto a glow-
1108 discharged (20 mA for 30 sec) holey-carbon grid (Quantifoil R2/2, copper, mesh 300) coated
1109 with continuous carbon (of ~3 nm thickness) and incubated for 30 sec in a controlled
1110 environment of 100% humidity and 4 ºC. The grids were blotted for 3 sec, followed by plunge-
1111 freezing in liquid ethane, using a Vitrobot MKIV (FEI/Thermofischer). For high resolution
1112 mitoribosome analysis, five separate datasets were collected on FEI Titan Krios
1113 (FEI/Thermofischer) transmission electron microscope operated at 300 keV, using C2 aperture of
1114 70 µm and a slit width of 20 eV on a GIF quantum energy filter (Gatan). A K2 Summit detector
1115 (Gatan) was used at a pixel size of 0.83 Å (magnification of 165,000X) with a dose of 29-32
1116 electrons/$Å^2$ fractionated over 20 frames. A defocus range of -0.6 to -2.8 µm was used. More
1117 detailed parameters for each one of the datasets are listed in Supplementary Table 1.

1118

1119 Cryo-EM data processing

1120 The complete workflows of the mitoribosomal complexes A/A-P/P-E/E, A/P-P/E, L1 stalk,
1121 monosome consensus map, SSU and their 8 masked regions are given in Extended Data Figs. 1
1122 and 2. For all the datasets, beam-induced motion correction and per-frame B-factor weighting
1123 were performed for all data sets using RELION-3.0.2 [36, 37]. Motion-corrected micrographs were
1124 used for contrast transfer function (CTF) estimation with gctf [94]. Unusable micrographs were
1125 removed by manual inspection of the micrographs and their respective calculated CTF
1126 parameters. Particles were picked in RELION-3.0.2 [36, 37] , using reference-free followed by
1127 reference-aided particle picking procedures. Reference-free 2D classification was carried out to
1128 sort useful particles from falsely picked objects, which were then subjected to 3D classification.
1129 3D classes corresponding to unaligned particles and LSU were discarded and monosome
1130 particles were pooled and used for 3D auto-refinement yielding a map with an overall resolution
1131 of 2.9-3.4 Å for the five datasets. Resolution was estimated using a Fourier Shell Correlation cut-
1132 off of 0.143 between the two reconstructed half maps. Finally, the selected particles were
1133 subjected to per-particle defocus estimation, beam-tilt correction and per-particle astigmatism

correction followed by Bayesian polishing. Bayesian polished particles were subjected to a second round per-particle defocus correction. A total of 994,919 particles from all datasets were then pooled and separated into 86 optics groups in RELION-3.1 [38], based on acquisition areas and date of data collection. Beam-tilt, magnification anisotropy and higher-order (trefoil and fourth-order) aberrations were corrected in RELION-3.1 [38]. Subsequently, 509,691 particles from datasets 2-4 were pooled together and subjected to 3D auto-refinement giving a final nominal resolution of 2.21 Å. Masked refinement was performed on the small subunit head, body, mS39 and tail to produce maps of 2.36 Å, 2.31 Å, 2.44 Å and 2.45 Å resolution, respectively and likewise for the SLU body, L10-L7/L12 stalk, CP and L1 stalk to yield maps of 2.08 Å, 2.38 Å, 2.36 Å and 2.89 Å resolution, respectively. To improve the quality of the L1-stalk map, 220,906 monosome particles with high occupancy of E/E-tRNA were pooled and subjected to partial signal subtraction using the mask that retains the E/E-tRNA and L1-stalk, followed by 3D auto-refinement to have a nominal resolution of 2.87 Å (Supplementary Fig. 1 and Supplementary Table 1).

For separating the A/A-P/P-E/E and A/P-P/E states, all 994,919 monosome particles were subjected to signal subtraction using the mask that retains the tRNA binding region. The tRNA binding sites displayed weak densities corresponding to a heterogeneous mixture of tRNAs bound with partial occupancy. Signal subtracted particles were 3D classified without alignment using a mask on the A-site. This yielded two main classes, one with density in the A-site (332,187 particles) and the other lacking it (629,597 particles). Particles with density in the A-site were selected and subjected to a second round of 3D-classification using a mask around the P- and E-sites. Two classes were selected, one with P/P- and E/E-tRNA density and other in hybrid state with P/E-tRNA density. All 3D classifications with signal subtracted particles were performed using a T-value of 400. The subtracted signal was reverted for these two classes, corresponding to the A/A-P/P-E/E state (82,522 particles) and A/P-P/E state (20,143 particles). Following 3D auto-refinement, the nominal resolution of the cosmplexes was 2.63 Å and 2.98 Å, respectively. Masked refinement for the classical state was performed using local masks on SSU head, body, tail, and mS39 to produce maps at 2.72 Å, 2.75 Å, 2.91 Å and 2.93 Å resolution, respectively. For the LSU body, L10-L7/L12, CP, and the L1 stalk regions, the resolution was 2.44 Å, 2.84 Å, 2.78 Å and 3.20 Å, respectively. Masked refinement for the hybrid state was performed using the same local masks as for the classical state but transformed to compensate for the structural differences. This produced maps for the SSU head, body, tail, and mS39 to produce maps of 3.03 Å, 3.07 Å, 3.39 Å and 3.47 Å resolution, respectively. For the LSU body, L10-L7/L12 region, CP, and the L1 stalk masks, the resolution was 2.84 Å, 3.29 Å, 3.25 Å and 3.53 Å, respectively. The maps were then subjected to modulation transfer function correction, automatic *B*-factor sharpening and local resolution filtering using RELION-3.1 (Supplementary Fig. 2, Supplementary Table 1).

1173 Model building and refinement

1174 We started by building a model into the 2.21 Å resolution consensus map. The starting model for
1175 the LSU was taken from PDB ID: 6ZSG, and for the SSU from PDB ID: 6RW4. These models
1176 were rigid body fitted using UCSF Chimera [95]. Individual local-masked refined maps with local-
1177 resolution filtering and *B*-factor sharpening (RELION 3.1) superposed to the overall map were
1178 combined into a single composite map using Phenix.combine_focused_maps [96] for model
1179 building and refinement. *Coot* v0.9 [97] with Ramachandran and torsion restraints was used for
1180 model building.

1181 The L1-stalk model was built using the 2.87 Å resolution masked-refined map of L1 stalk from
1182 E/E-tRNA-containing particles. Initial model for uL1m was generated by homology-modeling
1183 with uL1 structure of *T. thermophilus* (PDB ID: 3U4M) as template using the Swiss-Model
1184 webserver [98]. The N-terminal extension of uL1m (residues 61–93), the C-terminal domain
1185 (residues 158–254) and the preceding loop (residues 148–157) of uL9m, and H76-77 (residues
1186 2761–2786) of 16S rRNA were modeled manually into the density. Mitochondria-specific C-
1187 terminal extension of uL9m was modeled as a helix based on the density and secondary structure
1188 prediction by PSIPRED [99]. The model was rigid body fitted into the respective local-masked
1189 refined maps for L1 stalk region in the A/A P/P E/E and A/P/E states followed by self-restrained
1190 real space refinement in *Coot* v0.9.

1191 In the CP, the $tRNA^{Val}$ could be completely modeled, owing to the improved resolution of the
1192 local masked-refined map (2.36 Å). The 3′-CCA terminus (C74–A76) and a valine residue linked
1193 to A76 could be placed on the density map. The N-terminus of mL40 was extended by 13-
1194 residues (47–59) modeled in a tubular wedged between the A- and P-site tRNAs to the phosphate
1195 backbone of mRNA residue 7. Similarly, the C-terminus of bL31m was extended by 31 residues
1196 (95–125) from the C-terminal helix onto SSU head. The local resolution was sufficient for
1197 accurate side-chain modeling for most residues and secondary-structure assignments. We
1198 modeled a disulfide linkage between C45-C76 of mS37. However, they might exist in both
1199 disulfide-linked, and reduced states as indicated by the density and a water mediated hydrogen
1200 bond with a neighbouring Arginine side chain (R240 from uS7m). The other pair C55-C66
1201 appears to be reduced. However, as we had added 1mM DTT to our ribosome purification
1202 buffers, this is not truly indicative of the native state of C45-C76 or C55-C66 pairs.

1203 At the mRNA channel entrance, a more accurate and complete model of mS39 could be built
1204 with 29 residues added to the structure. Improved local resolution enabled unambiguous
1205 assignment of residues to the density which allowed us to address errors in the previous model.
1206 Finally, a total of 28 α-helices could be modeled in their correct register and orientation. Further,
1207 a 28-residue long N-terminal loop of mS31 (residues 247–275) along mS39 and mitochondria-
1208 specific N-terminal extension of uS9m (residues 53–70) approaching mRNA were modeled
1209 manually by fitting the loops into the density maps.

1210 Polyamines were identified upon a further manual inspection of the density map for the presence
1211 of continuous tubular densities which corresponded to spermine, spermidine or putrescine in

1212 length. A total of one spermine, four spermidines and one putrescine were placed in the model,
1213 justified by the electrostatic and hydrogen-bonding interactions that each polyamine exhibits at
1214 its amine groups with its neighbors.

1215 Metal ions, Mg^{2+}, K^{+} and Zn^{2+}, were modeled into densities based on a manual inspection of
1216 small density blobs and the chemical environment, specifically, coordination geometry and
1217 strength of density in both unsharpened and local resolution filtered maps. The coordination
1218 distance of Mg^{2+} is around 2 Å with an octahedral geometry, whereas that of K^{+} is around 3 Å
1219 with more relaxed constraints on coordination geometry. Notably, a density that was modeled
1220 previously as Zn^{2+} coordinated by residues D224, D240, D241 and H93 of uS2m was assigned as
1221 a magnesium ion, indicated by the octahedral geometry of coordination with the uS2m residues
1222 mentioned above and two water molecules.

1223 A-, P- and E-site tRNAs, and mRNA were modeled manually in the density. The density for
1224 tRNAs and mRNAs comes from a natively-bound heterogeneous population. Hence, individual
1225 residues were modeled as one of the nucleotides, A, U, G, or C, based on the density and/or
1226 conservation. While the 70 residues of P-site tRNA could be modeled, fewer residues could be
1227 modeled for the A-site (22 residues) and E-site tRNAs (43 residues), including the acceptor arm
1228 and anticodon loop due to weaker respective densities. Along the mRNA channel, 34 residues of
1229 mRNA were built. In the tRNA binding region, codon-anticodon pairs were clearly resolved.
1230 Additionally, extra residues near the A-site (10-12, 14-16) and at the mRNA channel entrance
1231 (25, 27-29) were modeled accurately into density. For the remaining mRNA chain at a relatively
1232 lower resolution, correct overall chain trace and nucleotide orientation could be assigned. This
1233 allowed specific protein-nucleotide interactions to be identified for uS5m, uS7m, uS9m, uS12m,
1234 mS35, mS39 and mL40.

1235 For modeling the classical A/A P/P E/E- and hybrid A/P P/E-states, the LSU and SSU from the
1236 consensus model were fitted into their composite maps, followed by manual revision. As
1237 described above, tRNAs and mRNA were modeled manually into the density.

1238 The water molecules were automatically picked by *Coot* v0.9 [62], followed by manual revision.
1239 Geometrical restraints of modified residues and ligands used for the refinement were calculated
1240 by Grade Web Server (http://grade.globalphasing.org) or obtained from CCP4 library [100].
1241 Hydrogens were added to the models except for water molecules by REFMAC5 [101] using the
1242 prepared geometrical restraint files. Charged α-amino-group hydrogens (H2 and H3) and a free-
1243 ribose hydrogen HO3′ were removed from non-terminal protein and RNA residues, respectively,
1244 while those at terminal residues were kept. Protonation of Histidine residues were judged based
1245 on the chemical environment and removed or kept their N-H hydrogens (HD1 and HE2)
1246 accordingly. Protonation/deprotonation of ligands and modified residues were also adjusted.

1247 Final models were further subjected to refinement with Phenix.real_space_refine v1.13_2998 [96],
1248 wherein three macro-cycles of global energy minimization with reference restraints (using the
1249 input model as the reference, sigma 5-7) and secondary structure restraints, rotamer restraints but
1250 without Ramachandran restraints were carried out for each model. The composite maps were

1251 used as the targets for the refinement. An 'edit' file that defines metal-coordination bonds was
1252 generated by ReadySet in the Phenix suite and used. Non-canonical covalent bonds, which are
1253 those between $tRNA^{Val}$ and Valine and between 1-methyl-isoaspartate 184 and G185 in uS11m,
1254 were also defined in the 'edit' file. Model refinement data are listed in Supplementary Table 1.

1255

1256 Bioinformatic analysis of the Y-N-C-Y motif

1257 The density and base-specific interactions of mRNA residues 25-28 with mS39 imply a sequence
1258 of pyrimidine, any nucleotide, cytosine, pyrimidine, leading to a consensus motif: Y-N-C-Y. We
1259 explored the possibility of increased frequency of this motif in mRNA sequences. The sequences
1260 for all 13 mRNAs were obtained from GenBank. The consensus motif was searched in each
1261 sequence and all occurrences (including ones that overlap) were recorded and used to calculate
1262 the percentage frequency of occurrence for each transcript and the average percentage frequency.
1263 To determine if there is an enrichment of this motif in mRNAs, we calculated its occurrence in a
1264 set of nuclear-encoded mRNAs. To create this set, we acquired sequences randomly from
1265 GenBank and subjected them to a 90% redundancy cut-off, resulting in a total of 1369
1266 sequences. The percentage frequency of occurrence of Y-N-C-Y motif was determined for each
1267 of the 1370 sequences and used to calculate an average percentage frequency for the entire set.
1268 Next to determine the distribution of the Y-N-C-Y motif across the length of mRNAs, each
1269 occurrence was plotted against its position number in the mRNA sequence. This distribution for
1270 all 13 mRNA sequences was plotted together for comparison.

1271

1272 Molecular Dynamics simulations: Modified force fields for simulating a truncated mL64 protein
1273 and modified interactions with protein uL1m

1274 *Baseline force field used for simulations of P/E formation*

1275 An all-atom multi-basin structure-based "SMOG" model [60, 61] of the mitoribosome was used to
1276 simulate P/E formation. For this, we first constructed single-basin structure-based models for the
1277 pre- and post-translocation configurations (A/A-P/P and P/P-E/E). We then combined the two
1278 models, such that the composite model stabilizes both the pre- and post-translocation
1279 configurations. Here we describe the baseline model, which is described in the main text. In
1280 subsequent sections, we provide detailed descriptions of all modified force fields.

In a single-basin all-atom structure-based model, every non-hydrogen atom is represented by a bead of unit mass, and an experimentally-obtained structure is used to define the potential energy minimum. The functional form of the potential is given by:

$$U = \sum_{\text{bonds}} \frac{\epsilon_r}{2}(r_i - r_{i,0})^2 + \sum_{\text{angles}} \frac{\epsilon_\theta}{2}(\theta_i - \theta_{i,0})^2$$

$$+ \sum_{\text{impropers}} \frac{\epsilon_{\chi_{imp}}}{2}(\chi_i - \chi_{i,0})^2 + \sum_{\text{planars}} \epsilon_{\chi_{planar}}[1 - \cos(2\chi_i)]$$

$$+ \sum_{\substack{\text{backbone}\\\text{dihedrals}}} \epsilon_{bb} F(\phi_i - \phi_{i,0}) + \sum_{\substack{\text{sidechain}\\\text{dihedrals}}} \epsilon_{sc} F(\phi_i - \phi_{i,0})$$

$$+ \sum_{\text{contacts}} \epsilon_c \left[\left(\frac{\sigma_{ij}}{r_{ij}}\right)^{12} - 2\left(\frac{\sigma_{ij}}{r_{ij}}\right)^{6} \right] + \sum_{\text{non-contacts}} \epsilon_{nc} \left(\frac{\sigma_{nc}}{r_{ij}}\right)^{12}$$

where

$$F(\phi) = [1 - \cos(\phi)] + \frac{1}{2}[1 - \cos(3\phi)]$$

r_0 and θ_0 parameters are assigned values found in the Amber ff03 force field [102]. The dihedral parameters ϕ_0 are defined by the experimental structure. χ_0 non-planar improper dihedrals (around chiral centers) are also defined to have the values adopted in the experimental structures. Planar dihedral angles are given a cosine term with periodicity 2 and minima at 0 and 180 degrees. The energy scale is set to $\epsilon_r = 100\frac{\epsilon}{A^2}, \epsilon_\theta = 80\frac{\epsilon}{rad^2}, \epsilon_{\chi_{imp}} = 10\frac{\epsilon}{rad^2}, \epsilon_{\chi_{planar}} = 40\frac{\epsilon}{rad^2}$, where ϵ is the reduced energy scale. The dihedral and contact energy scales $\epsilon_{bb}, \epsilon_{sc}, \epsilon_C$ are normalized as in Ref. [60].This combination of structure-based non-bonded terms and AMBER bonded terms is identical to the implementation of a previous SMOG-amber variant (called SBM_AA-amber-bonds [103] in the SMOG 2 force field repository (smog-server.org), though post-transcriptionally-modified residues were added for the current model. Upon publication, the SMOG 2 force field templates used in the current study will be available for download on the SMOG 2 force field repository (ID: AA_PTM_Hassan21.v1).

For the non-bonded interactions, each atomic contact that is found in the experimental structure (i.e. "native'' contact) is given an attractive Lennard-Jones-like interaction that stabilizes a preassigned structure. Native contacts were defined based on the Shadow Contact Map algorithm with default parameters [104]. Σ_{ij} are the interatomic distances between contacts in the native structure, multiplied by 0.96. As employed previously in simulations of the ribosome [105, 106] and viral capsids [103], this scaling of the contact distance was employed to avoid artificial expansion of the ribosome that results from thermal energy. That is, while the potential energy is defined such that the experimental structure is the global minimum, thermal energy leads to a free-energy minimum for which the ribosome is slightly expanded. By shortening the stabilizing interactions, the free-energy minimum is consistent with the experimental structure. For this comparison, the radius of gyration (R_g) was used as a measure of expansion. With this scaling of the contact

distances, R_g was found to match that of the cryo-EM model. All non-native contacts are given a repulsive term that ensures excluded-volume steric interactions are present. The parameter σ_{nc} is given the value 2.5 Å, while $\epsilon_{nc} = 0.1\epsilon$.

Stabilizing intra-ribosome contacts and dihedrals were assigned the values found in the A/P-P/E (SSU rotated) hybrid structure, which is described in the main text. This ensures that the SSU rotates forward in each simulation. Each simulation is initiated from the A/A-P/P conformation. All intra-mt-tRNA and intra-mt-mRNA contacts were defined based on the A/A-P/P structure. Since stabilizing contacts in a structure-based model describe effective interactions [107, 108], we rescaled the strengths of subsets of contacts within the model. Consistent with recent simulations of P/E formation in bacteria [105], interactions that stabilize the structure of the ribosome (i.e. intra-ribosomal) are given larger weights than contacts that are only transiently-formed (e.g. tRNA-ribosome contacts). Relative to intra-ribosome contacts, the energetic interactions between the mt-mRNA-tRNA complex and the SSU (in A/A-P/P and P/P-E/E structures) were rescaled by a factor of 0.3. While these interactions were weaker than intra-ribosomal contacts, since the simulations were not performed under conditions in which translocation will occur (*e.g.*, binding of elongation factors or back-rotation, etc), the mt-mRNA maintained its initial position on the mRNA track of the SSU. P/P-E/E contacts between the mt-tRNA and the uL1m protein were rescaled by a factor of 0.8 and all other interactions between mt-mRNA-tRNA and the LSU were rescaled by a factor of 0.1. This rescaling was applied to account for the transient nature of mt-mRNA-tRNA binding to the ribosome. The strength of the uL1m-tRNA contacts was set such that the P/E configuration would stably form contacts with the uL1m protein. When contacts were scaled below a factor of ~0.5, we found that uL1m could not form stable interactions with the mt-tRNA.

Interactions between the 3′-CCA ends of A-site and P-site mt-tRNAs with the A-site and the P-site were scaled by a factor of 0.2, while their interactions with P-site and E-site were scaled by a factor of 0.8. This leads to the mt-tRNA molecules favoring binding of their target sites (*i.e.*, sites bound in the P/E configuration) on the ribosome. While the interactions with the subsequent binding site (*i.e.*, A-site mt-tRNA with the P-site and P-site mt-tRNA with the E-site) were stronger, these contacts are short range (~6 Å). Accordingly, the stronger weights do not affect the dynamics of the mt-tRNA until it is very close to the binding site. Thus, the details of the final repositioning of the 3′-CCA tail of the P-site mt-tRNA should not be overinterpreted. While the contacts are short-range, the structure of the mitoribosome may introduce steric barriers that the mt-tRNA must navigate in order to adopt the P/E configuration [108]. With these considerations in mind, the current model is aimed at identifying structural elements that can impose steric limitations on mt-tRNA during P/E formation.

There were also two sets of harmonic potentials that were introduced. To mimic the presence of a nascent peptide chain, which would restrain the 3′-CCA end of the A-site tRNA to the PTC, we introduced weak harmonic restraints (weight of $1/nm^2$) between the 3′-CCA end of the A-site tRNA and the P site of the LSU. Distances were assigned based on the P/P conformation. These weak interactions ensured that the 3′-CCA end remains localized to the PTC. We also

introduced harmonic potentials between base-pairing contacts in the mt-tRNA acceptor arm (weight 1000/nm^2). Due to the details of the contact map, initial simulations exhibited partial unfolding/refolding of the acceptor arm during P/E formation. Since that was likely an artifact due to the simplicity of the model and the details of the contact map definition, these additional harmonic terms were introduced to ensure the tRNA acceptor arm remained folded throughout the transition.

Modified force fields

Multiple variants of the model (*i.e.*, force field) were considered, in order to investigate the influence of steric interactions between the P-site mt-tRNA and C-terminal residues of mL64 and to investigate the influence of attractive interactions between uL1m and P-site mt-tRNA on P/E formation.

Truncated-mL64 model: ΔmL64 force field

The C-terminal region of mL64 is involved in steric interactions with the mt-tRNA. For ΔmL64 model, the C-terminal region of mL64 (beginning with Q112) was removed from the system. Q112 was chosen as truncating here guarantees no steric interactions between mL64 and the mt-tRNA and keeps the rest of the protein intact. Thus, all other interactions were unperturbed. This model is intended to mimic an ideal experiment, where one could delete the terminal region of mL64 without introducing indirect effects on the dynamics. In our application, this model allows us to ask what effect steric interactions between P-site mt-tRNA elbow and mL64 have on the dynamics of P/E formation. Deletion of this region from the model was achieved using the smog_extract tool of the SMOG 2 software package [60].

Modified-uL1m model: ΔuL1m force field

All stabilizing contacts between uL1m and the P-site mt-tRNA that are formed in the P/P-E/E state were scaled by a relative factor of 0.1, rather than 0.8 (baseline model, above). Thus, by weakening the attractive interactions, there is insufficient stabilizing energy between uL1m and the P/E tRNA, such that the tRNA elbow does not fully reach the P/E configuration.

Combined truncated mL64 and modified uL1m model: ΔmL64-ΔuL1m force field

All modifications applied in the truncated mL64 model and the modified-uL1m model were included in a single combined force field.

Simulation details

All simulations were initiated from the pre-translocation A/A-P/P configuration. All force field files were generated using the SMOG 2 software package [60]. Molecular dynamics simulations

1384 were performed using Gromacs (v5.1.4) [109, 110]. Reduced units were used in all calculations.
1385 Energy minimization was first performed using steepest descent minimization. The system was
1386 then coupled to a heat bath using Langevin Dynamics protocols, with reference temperature of
1387 0.5 ε/k_B reduced temperature units (60 Gromacs units). This temperature was chosen since it has
1388 been shown to produce structural fluctuations that are consistent with those inferred from
1389 anisotropic *B*-factors and explicit-solvent simulation [111]. The timestep was 0.002 reduced units
1390 and each simulation was continued until the distance of the 3'-CCA end from the LSU E-site
1391 R_{CCA} reached a value less than 4 Å. Energy minimization was initially performed using steepest
1392 descent minimization. Each simulation was performed for a maximum of 10^8 timesteps. For the
1393 primary/baseline model described in the main text (327 simulations) we obtained an aggregate
1394 simulated time of 2.27 $*10^6$ reduced units. For the truncated mL64 model (ΔmL64 model) (321
1395 simulations), the aggregate simulation time was 1.87 $*10^6$ reduced units. For the attenuated uL1m
1396 contacts model (ΔuL1m model) (237 simulations), the aggregate simulation time was 1.76 $*10^6$
1397 reduced units. For the ΔmL64-ΔuL1m model (181 simulations), the aggregate simulation time
1398 was 1.04 * 10^6. Previous comparisons of diffusion coefficients of tRNA molecules in the
1399 ribosome (explicit-solvent simulations vs. SMOG models), estimate that 1 reduced unit
1400 corresponds to an effective timescale of approximately 1 nanosecond [112]. Using this conversion
1401 factor, the presented simulations represent an aggregate effective simulate time of ~ 6.94
1402 milliseconds.

1403 *Structural metrics for describing simulated dynamics*

1404 - A-site mt-tRNA, R^P_{CCA}: distance between the geometric centers of the side chains of C75 in the
1405 A-site mt-tRNA and Gm2815 in the LSU rRNA. These residues base pair in the A/P-P/E and
1406 P/P-E/E configurations.

1407 - P-site mt-tRNA, R^P_{CCA}: distance between the geometric centers of the side chains of C75 in the
1408 P-site mt-tRNA and Gm2815 in the LSU rRNA. These residues base pair in the A/P-P/E
1409 configuration.

1410 -R_{CCA}: distance between the geometric centers of the side chains of A76 in the P-site mt-tRNA
1411 and G2909 in the LSU rRNA. G2909 in the E-site forms a base stacking interaction with A76 of
1412 P-site mt-tRNA in the A/P-P/E configuration.

1413 -R_{elbow}: distance between geometric centers of U54 of P-site mt-tRNA and its reference position
1414 in the A/P-P/E configuration after alignment of the LSU rRNA.

1415 - $Q_{\mathrm{L1-tRNA}}$: the fraction of P/P-E/E contacts between uL1m and P-site mt-tRNA. A contact is
1416 defined as formed if it is within a factor of 1.2 of the distance found in the P/P-E/E configuration.

1417

1418 *SSU rotation and tilt angles*

1419 To follow the rotary motions of the SSU body with respect to the LSU, we calculated rotation
1420 and tilt angles for both the SSU body. For this, we first determined the corresponding *E. coli*
1421 numbering of the mitoribosome rRNA residues via STAMP alignment [113] of the mitoribosome to

1422 a reference *E. coli* structure (PDB ID: 4V9D). Alignment was performed separately for the LSU,
1423 SSU head and SSU body. The angles were then calculated, using the assigned *E. coli* numbering.
1424
1425 *Structural model preparation for simulations*
1426 Since the cryo-EM models did not resolve the exact same set of atoms, there was a need to
1427 perform some additional structural models prior to performing simulations. For example, to
1428 define the multi-basin structure-based model, it was necessary for each mt-tRNA molecule to
1429 have identical atoms in the pre- and post-translocation configurations. Additionally, to define
1430 the intra-ribosome interactions to stabilize the A/P-P/E conformation, it was necessary that all
1431 mt-rRNA and mitoribosomal proteins had identical atomic composition. While most of the
1432 resolved atoms are common to all reported models, we employed restraint-based modeling to
1433 construct models of the mitoribosome and mt-tRNA that have identical compositions. Below, we
1434 describe the steps required for modeling the mitoribosome and mt-tRNA.
1435
1436 *Structural modeling pre-processing steps for rRNA and proteins for simulations*
1437 Since the structure-based model only included intra-ribosome interactions from the A/P-P/E
1438 structure, we first removed all mt-tRNA and mt-mRNA from the A/A-P/P and A/P-P/E models.
1439 We also removed ligands and water molecules (HOH, SPD, PUT, NAD, SPM). For the
1440 remaining atoms, we identified all atoms that were common to the A/A-P/P and A/P-P/E
1441 structures. We then generated a single-basin structure-based model of the A/A-P/P structure.
1442 Next, position restraints (harmonic terms, weight of 100 for each atom) were introduced for all
1443 common atoms, with positions corresponding to the A/P-P/E structure. The system was then
1444 energy minimized via steepest descent minimization. Then, the system was subject to simulated
1445 annealing. The system was initially simulated at 0.15 reduced temperature units for 25,000
1446 timesteps. The temperature was then linearly decreased to 0 over the next 50,000 timesteps. An
1447 additional 25,000 steps were simulated at temperature 0. The final, annealed structural model
1448 was used for force field generation steps, as described above.
1449
1450 *Structural modeling pre-processing steps for mt-tRNA and mt-mRNA*
1451 Since the cryo-EM reconstructions reported consensus/average sequences for each mt-tRNA, the
1452 composition of the A-, P- and E-site mt-tRNAs were not identical. To perform simulations, we
1453 homogenized the composition of the mt-tRNA molecules in the A/A-P/P-E/E structure and the
1454 mt-tRNA codons. For this, we started with the structural model of the A-site mt-tRNA (and the
1455 associated codon) from the A/A-P/P structure, and then used it to generate a structure-based
1456 model. We then introduced position restraints based on the positions of the A-site mt-tRNA in
1457 the A/A-P/P-E/E structure. All common atoms (*i.e.*, backbone atoms, or atoms in identical
1458 residues) were restrained to the A-site mt-tRNA/mRNA positions. For the A-site mt-tRNA,
1459 restraints were not imposed on residues 46-58 and 16-17. Cycles of minimization and annealing

1460 were performed, where the position restraints were given weights of 1, 10, 100 and then 1000.
1461 This process was repeated for the P-site and E-site mt-tRNAs, as well as for the upstream and
1462 downstream mt-mRNA. This process produced a model of the A/A-P/P-E/E configuration that
1463 has repeating codons and identical mt-tRNA composition. This structural model was used to
1464 define the pre-translocation and post-translocation structure-based models, which were used to
1465 construct the multi-basin model.

1466 *Describing the sequence of rearrangements in simulations*

1467 To describe the dynamics of the P-site mt-tRNA during P/E state formation, we have defined
1468 three states based on the 2D probability distribution of R^E_{elbow} and R^E_{CCA} distances (Fig. 8). These
1469 states are defined as all configurations of the P-site mt-tRNA in the baseline model that sample
1470 the following values of R^E_{elbow} & R^E_{CCA}:
1471 state I_1: disk centered at (R^E_{elbow},R^E_{CCA})=(46,35) Å with radius r=6 Å
1472 state I_2: disk centered at (R^E_{elbow},R^E_{CCA})=(63,23) Å with radius r=8 Å
1473 state I_3: disk centered at (R^E_{elbow},R^E_{CCA})=(42,13) Å with radius r=7 Å
1474

1475 Using this definition of the intermediate states, the most common sequence of transitions
1476 followed the order P/P => I_1 => I_2 => I_3 => P/E.
1477

1478 Structure analysis and Fig.s

1479 Visualization and analysis of the models and maps was carried out using UCSF Chimera and
1480 ChimeraX [95, 114]. For model and map comparisons, models were superposed in *Coot* v0.9 [62] using
1481 the Secondary Structure Matching algorithm and maps downloaded from EMDB were resampled
1482 on our maps in UCSF Chimera. Simulated snapshots were visualized using Visual Molecular
1483 Dynamics [115].

1484

1485 Quantitation and statistical analysis

1486 All experiments were done in at least biological triplicate unless otherwise stated. GraphPad
1487 Prism 8 software was used for statistical analyses of the data. One-way analysis of variance
1488 (ANOVA) was performed, comparing the mean of each cell line with the mean of the mS29-KO
1489 cell line reconstituted with WT mS29, followed by Dunnett's multiple comparisons test. The
1490 data is presented as the mean ± SD; * $P \leq 0.05$, ** $P \leq 0.01$, *** $P \leq 0.001$, **** $P \leq 0.0001$. For
1491 immunoblotting, band density is quantified and normalized to ACTIN. For metabolic labeling of
1492 mitochondrially translated peptides in whole cells, the data presented represents the mean of each
1493 sample's ^{35}S signals.

1494

1495 **Additional References**

1496 86. Aibara S, Andrell J, Singh V, Amunts A. Rapid Isolation of the Mitoribosome from HEK
1497 Cells. *J Vis Exp*, (2018).

87. Morita E, Arii J, Christensen D, Votteler J, Sundquist WI. Attenuated protein expression vectors for use in siRNA rescue experiments. *Biotechniques* **0**, 1-5 (2012).

88. Yamauchi Y*, et al.* Denaturing reversed phase liquid chromatographic separation of non-coding ribonucleic acids on macro-porous polystyrene-divinylbenzene resins. *J Chromatogr A* **1312**, 87-92 (2013).

89. Nakayama H, Yamauchi Y, Taoka M, Isobe T. Direct identification of human cellular microRNAs by nanoflow liquid chromatography-high-resolution tandem mass spectrometry and database searching. *Anal Chem* **87**, 2884-2891 (2015).

90. Taoka M*, et al.* Landscape of the complete RNA chemical modifications in the human 80S ribosome. *Nucleic Acids Res* **46**, 9289-9298 (2018).

91. Taoka M*, et al.* The complete chemical structure of Saccharomyces cerevisiae rRNA: partial pseudouridylation of U2345 in 25S rRNA by snoRNA snR9. *Nucleic Acids Res* **44**, 8951-8961 (2016).

92. Bourens M, Barrientos A. A CMC1-knockout reveals translation-independent control of human mitochondrial complex IV biogenesis. *EMBO Rep* **18**, 477-494 (2017).

93. Leary SC, Sasarman F. Oxidative phosphorylation: synthesis of mitochondrially encoded proteins and assembly of individual structural subunits into functional holoenzyme complexes. *Methods Mol Biol* **554**, 143-162 (2009).

94. Zhang K. Gctf: Real-time CTF determination and correction. *J Struct Biol* **193**, 1-12 (2016).

95. Pettersen EF*, et al.* UCSF Chimera--a visualization system for exploratory research and analysis. *J Comput Chem* **25**, 1605-1612 (2004).

96. Afonine PV*, et al.* Real-space refinement in PHENIX for cryo-EM and crystallography. *Acta Crystallogr D Struct Biol* **74**, 531-544 (2018).

97. Emsley P, Cowtan K. Coot: model-building tools for molecular graphics. *Acta Crystallogr D Biol Crystallogr* **60**, 2126-2132 (2004).

98. Waterhouse A*, et al.* SWISS-MODEL: homology modelling of protein structures and complexes. *Nucleic Acids Res* **46**, W296-W303 (2018).

99. Buchan DWA, Jones DT. The PSIPRED Protein Analysis Workbench: 20 years on. *Nucleic Acids Res* **47**, W402-W407 (2019).

100. Krissinel EB, *et al.* The new CCP4 Coordinate Library as a toolkit for the design of coordinate-related applications in protein crystallography. *Acta Crystallogr D Biol Crystallogr* **60**, 2250-2255 (2004).

101. Murshudov GN, *et al.* REFMAC5 for the refinement of macromolecular crystal structures. *Acta Crystallogr D Biol Crystallogr* **67**, 355-367 (2011).

102. Duan Y, *et al.* A point-charge force field for molecular mechanics simulations of proteins based on condensed-phase quantum mechanical calculations. *J Comput Chem* **24**, 1999-2012 (2003).

103. Whitford PC, Jiang W, Serwer P. Simulations of Phage T7 Capsid Expansion Reveal the Role of Molecular Sterics on Dynamics. *Viruses* **12**, (2020).

104. Noel JK, Whitford PC, Onuchic JN. The shadow map: a general contact definition for capturing the dynamics of biomolecular folding and function. *J Phys Chem B* **116**, 8692-8702 (2012).

105. Levi M, Walak K, Wang A, Mohanty U, Whitford PC. A steric gate controls P/E hybrid-state formation of tRNA on the ribosome. *Nat Commun* **11**, 5706 (2020).

106. Nguyen K, Whitford PC. Steric interactions lead to collective tilting motion in the ribosome during mRNA-tRNA translocation. *Nat Commun* **7**, 10586 (2016).

107. Chan HS, Zhang Z, Wallin S, Liu Z. Cooperativity, local-nonlocal coupling, and nonnative interactions: principles of protein folding from coarse-grained models. *Annu Rev Phys Chem* **62**, 301-326 (2011).

108. Levi M, Noel JK, Whitford PC. Studying ribosome dynamics with simplified models. *Methods* **162-163**, 128-140 (2019).

109. Hess B, Kutzner C, van der Spoel D, Lindahl E. GROMACS 4: Algorithms for Highly Efficient, Load-Balanced, and Scalable Molecular Simulation. *J Chem Theory Comput* **4**, 435-447 (2008).

110. Lindahl E, Hess B, van der Spoel D. GROMACS 3.0: a package for molecular simulation and trajectory analysis. *Journal of Molecular Modeling* **7**, 306-317 (2001).

111. Jackson J, Nguyen K, Whitford PC. Exploring the balance between folding and functional dynamics in proteins and RNA. *Int J Mol Sci* **16**, 6868-6889 (2015).

112. Yang H, Bandarkar P, Horne R, Leite VBP, Chahine J, Whitford PC. Diffusion of tRNA inside the ribosome is position-dependent. *J Chem Phys* **151**, 085102 (2019).

113. Russell RB, Barton GJ. Multiple protein sequence alignment from tertiary structure comparison: assignment of global and residue confidence levels. *Proteins* **14**, 309-323 (1992).

114. Pettersen EF*, et al.* UCSF ChimeraX: Structure visualization for researchers, educators, and developers. *Protein Sci* **30**, 70-82 (2021).

115. Humphrey W, Dalke A, Schulten K. VMD: visual molecular dynamics. *J Mol Graph* **14**, 33-38, 27-38 (1996).

Data availability statement

The atomic coordinates were deposited in the RCSB Protein Data Bank, and EM maps have been deposited in the Electron Microscopy Data bank under accession numbers: 7QI4 and EMD-13980 (consensus monosome), 7QI5 and EMD-13981(classical state), 7QI6 and EMD-13982 (hybrid state).

The atomic coordinates that were used in this study: 3U4M (uL1 from *T. thermophilus*), 4V51 (*T. thermophilus* ribosome with mRNA, tRNA), 4V9D (*E. coli* ribosome), 4Y4P (*T. thermophilus* ribosome with A-, P-, E-site tRNAs), 6QNR (*T. thermophilus* ribosome with experimentally assigned K^+ ions) 6RW4 (mtSSU with mtIF3), 6ZM5 (mitoribosome from actinonin-treated cells) 6ZSG (mitoribosome with mRNA, tRNA), 6ZTJ (*E.coli* expressome), 6ZTN (*E.coli* expressome), 7K00 (*E. coli* ribosome at 2 Å resolution).

Acknowledgments

We thank the EMBO Young Investigator Program, the Northeastern University Discovery cluster and Northeastern University Research Computing staff. Swedish Foundation for Strategic Research (FFL15:0325), Ragnar Söderberg Foundation (M44/16), European Research Council (ERC-2018-StG-805230), Knut and Alice Wallenberg Foundation (2018.0080), Japan Science and Technology Agency (19198049), NIH-R35 grant (GM118141 to A.B.), and MDA Research Grant (MDA-381828 to A.B.). V.S. is supported by the Horizon 2020 - Marie Sklodowska-Curie Innovative Training Network (721757). Y.I. was supported by H2020-MSCA-IF-2017 (799399-Itohribo). The SciLifeLab cryo-EM facility is funded by the Knut and Alice Wallenberg, Family Erling Persson, and Kempe foundations. P.C.W. was supported by NSF grant MCB-1915843. Work at the Center for Theoretical Biological Physics was also supported by the NSF (Grant PHY-2019745). We would like to thank AMD for the donation of critical hardware and support resources from its HPC Fund that made this work possible.

Author contributions

V.S., Y.I., S.A., and J.A. collected cryo-EM data. V.S. and Y.I. processed the data and built the models. V.S., Y.I., R.K.F., A.N., S.A. and A.A. carried out structural analysis. Y.N., K.I. and M.T. performed mass-spec characterization. S.L.D. and A.B. performed biochemical characterization. A.H. and P.C.W. performed molecular simulations. All authors contributed to data interpretation and manuscript writing.

Competing Interests Statement

The authors declare no competing interests.

SUPPLEMENTARY INFORMATION

Table of contents:

Supplementary Fig. 1: Cryo-EM processing overview.

Supplementary Fig. 2: Resolution and model validation.

Supplementary Fig. 3: SILNAS of human mitoribosomal rRNA.

Supplementary Fig. 4: Complete rRNA sequence showing rRNA modifications determined by SILNAS.

Supplementary Fig. 5: Comparison of polyamine densities with antibiotic-treated cells (PDB ID 6ZM5).

Supplementary Fig. 6: Comparison of protein elements involved in mRNA binding with *E. coli*.

Supplementary Fig. 7: Frequency of Y-N-C-Y motif in the human mitochondrial mRNA transcripts.

Supplementary Fig. 8: Interactions of uS12m with codon in the A-site.

Supplementary Fig. 9: Mitoribosomal proteins involved in mRNA binding.

Supplementary Fig. 10: mRNA-rRNA interactions in the decoding center and roles of modifications.

Supplementary Fig. 11: Analysis of nucleotide binding by mS29 and its role in mitoribosome function.

Supplementary Table 1: Data collection and model statistics.

SI Video 1. The mRNA path and mitoribosome-specific components involved in mRNA recognition.

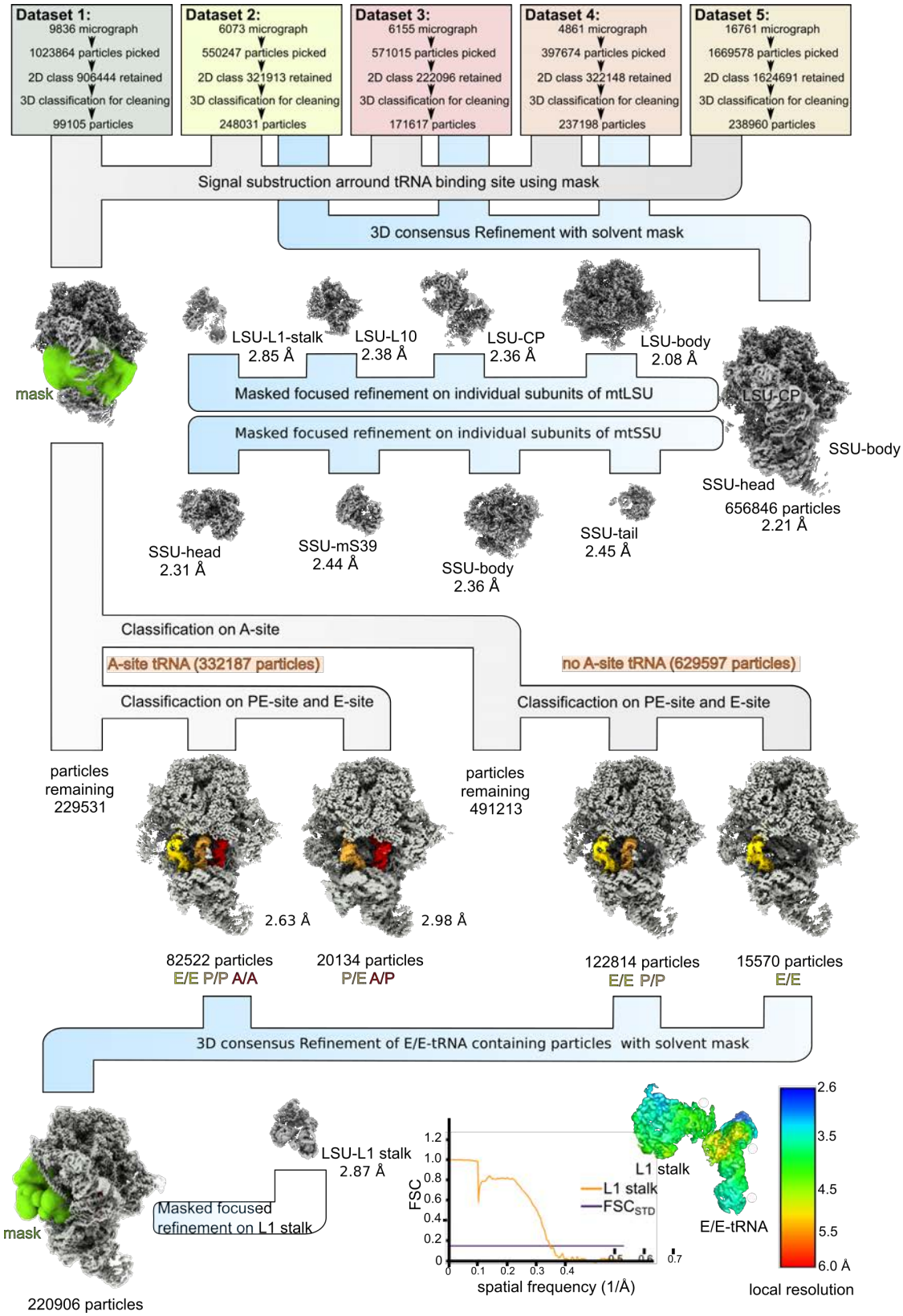

Supplementary Fig. 1: Cryo-EM processing overview.

Data processing scheme for classical (A/A P/P E/E) and hybrid (A/P P/E) states. Bottom panel, local-masked refinements, resolution and model validation for the L1 stalk. A total of 43686 movies were recorded and analyzed, particles that were not mitoribosomes were discarded by classification, since they cannot contribute to reconstruction. Consensus map was produced from 656846 particles. The classical A/A P/P E/E and hybrid A/P P/E maps were obtained from 82522 and 20134 particles, respectively. Cryo-EM structures were successfully obtained from 5 preliminary datasets.

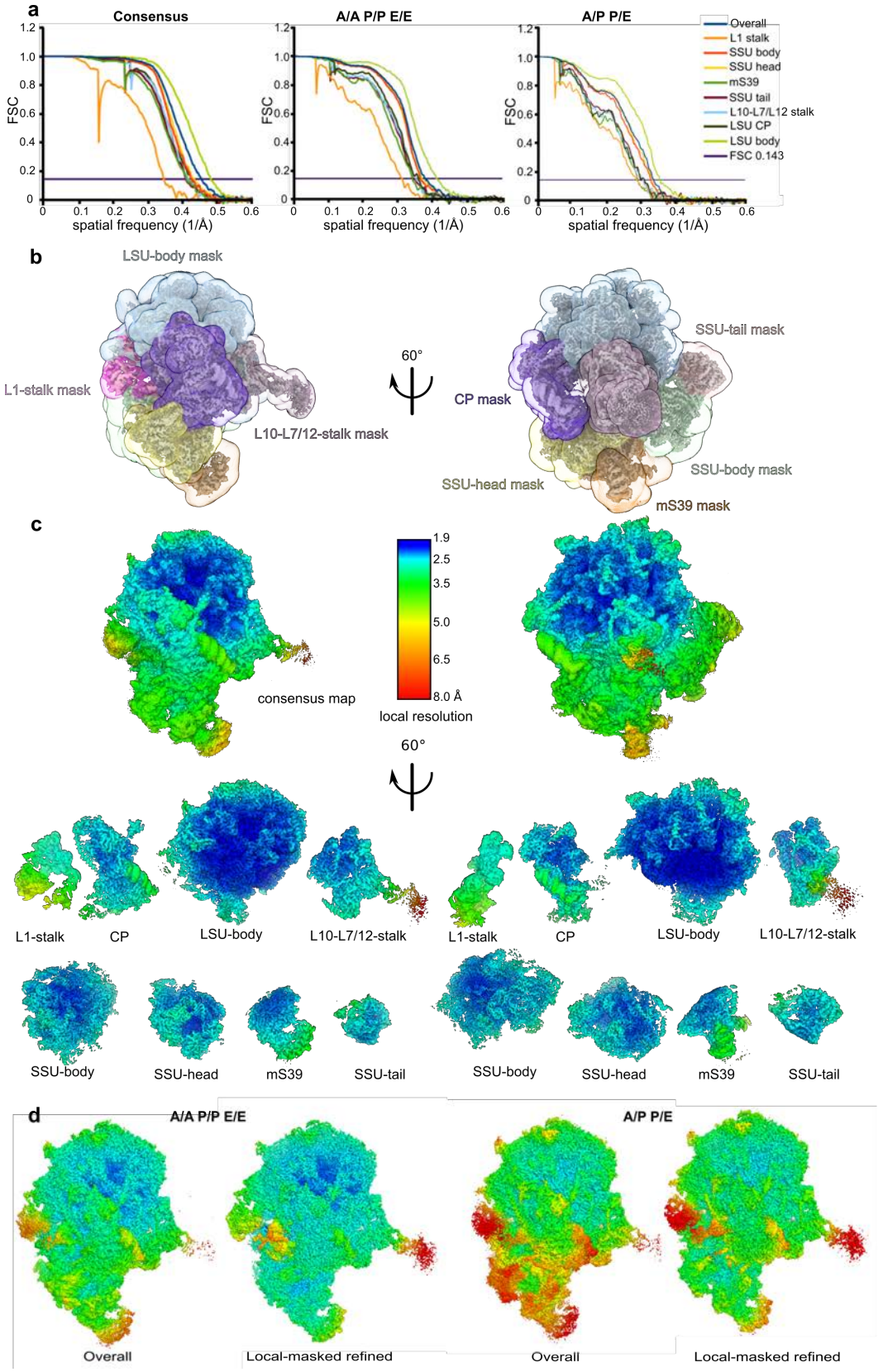

Supplementary Fig. 2: Resolution and model validation.
a, Fourier Shell Correlation curves of the half maps and local-masked refinements. **b,** Binary masks used for local-masked refinements. **c,** Local-masked refinements colored by local resolution. **d,** Overall maps for classical and hybrid states and their corresponding local-masked refined maps fitted and colored by local resolution. Cryo-EM map resolution estimates by Fourier Shell Correlation were performed using half- maps from random half-sets.

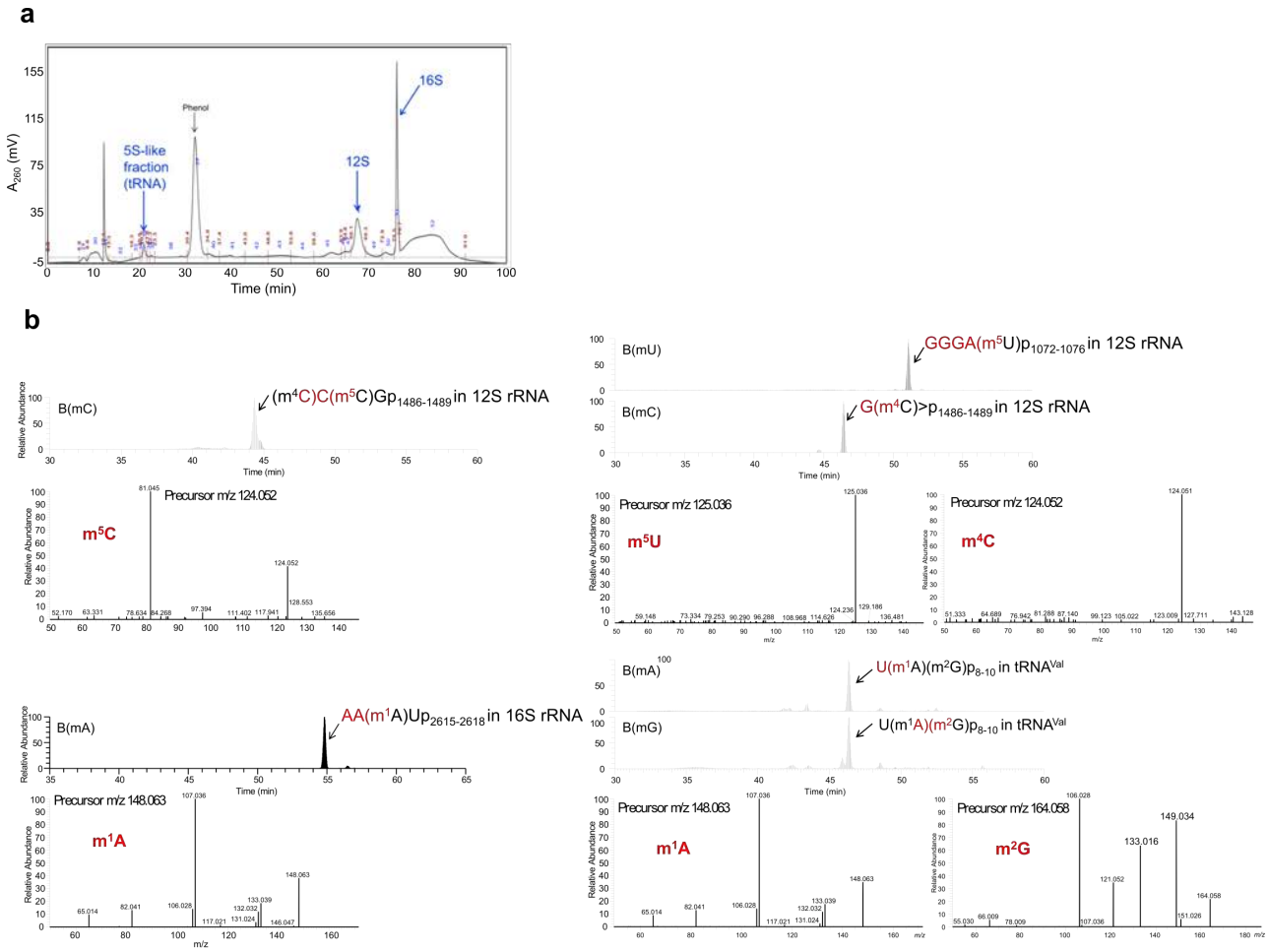

c

Genome # (NC_012920.1)	rRNA name	Position of PTM	rRNA modification name	Occupancy
1610	CP-tRNA^{Val}	9	1-methyladenosine	>78
1611	CP-tRNA^{Val}	10	N2-methylguanosine	>78
1638	CP-tRNA^{Val}	39	pseudouridine	89
838	12S rRNA	191	pseudouridine	17
946	12S rRNA	299	pseudouridine	18
1076	12S rRNA	429	5-methyluridine	97
1207	12S rRNA	560	pseudouridine	37
1257	12S rRNA	610	pseudouridine	29
1270	12S rRNA	623	pseudouridine	7
1486	12S rRNA	839	N4-methylcytidine	96
1488	12S rRNA	841	5-methylcytidine	94
1583	12S rRNA	936	N6,N6-dimethyladenosine	99
1584	12S rRNA	937	N6,N6-dimethyladenosine	99
2617	16S rRNA	947	1-methyladenosine	99
2815	16S rRNA	1145	2´O-methylguanosine	52
3034	16S rRNA	1364	pseudouridine	11
3039	16S rRNA	1369	2´O-methyluridine	96
3040	16S rRNA	1370	2´O-methylguanosine	100
3067	16S rRNA	1397	2´O-methyluridine	98

Supplementary Fig. 3: SILNAS of human mitoribosomal rRNA.
a. Reversed phase-LC isolation of the rRNAs extracted from the HEK 293 mitoribosome (10 µg) applied to a PLRP-S 4000A column (4.6 × 150 mm, 10 µm, Agilent Technologies). **b.** Selective detection and identification of mono-methylated nucleoside isomers in human mitochondrial

rRNAs. The HEK293 12S rRNA, 16S rRNA and CP-tRNA^{Val} (each 200 fmol) were digested with RNase T1 or RNase A, and the products subjected to LC-MS with an in-source fragmentation energy of 70 eV. The signals initially extracted for the second step were at m/z 148.06, 164.06, 125.04, and 124.05 (mass tolerance, +/-5 ppm) for B(mA), B(mG), B(mU) and B(mC), respectively. The extracted chromatograms of the oligonucleotides containing the mono-methylated nucleobase dissociated from RNase A and RNAse T1 digestion of the mitochondrial 12S rRNA (top left and top right panels) and 16S rRNA (bottom left and bottom right panels) are shown, respectively. Pseudo-MS3 spectra of the mono-methylated nucleobases are shown below each. The sequences assigned by Ariadne are shown next to their signals (arrow). The assigned mono-methylated isomers are shown in red. The spectrum was obtained from the m^2G anion of the oligonucleotide because the ratio of the signal heights at m/z 133.016 and 149.034 are 0.75. **c.** Table lists all the HEK 293 mt-rRNA modifications identified with their respective occupancies.

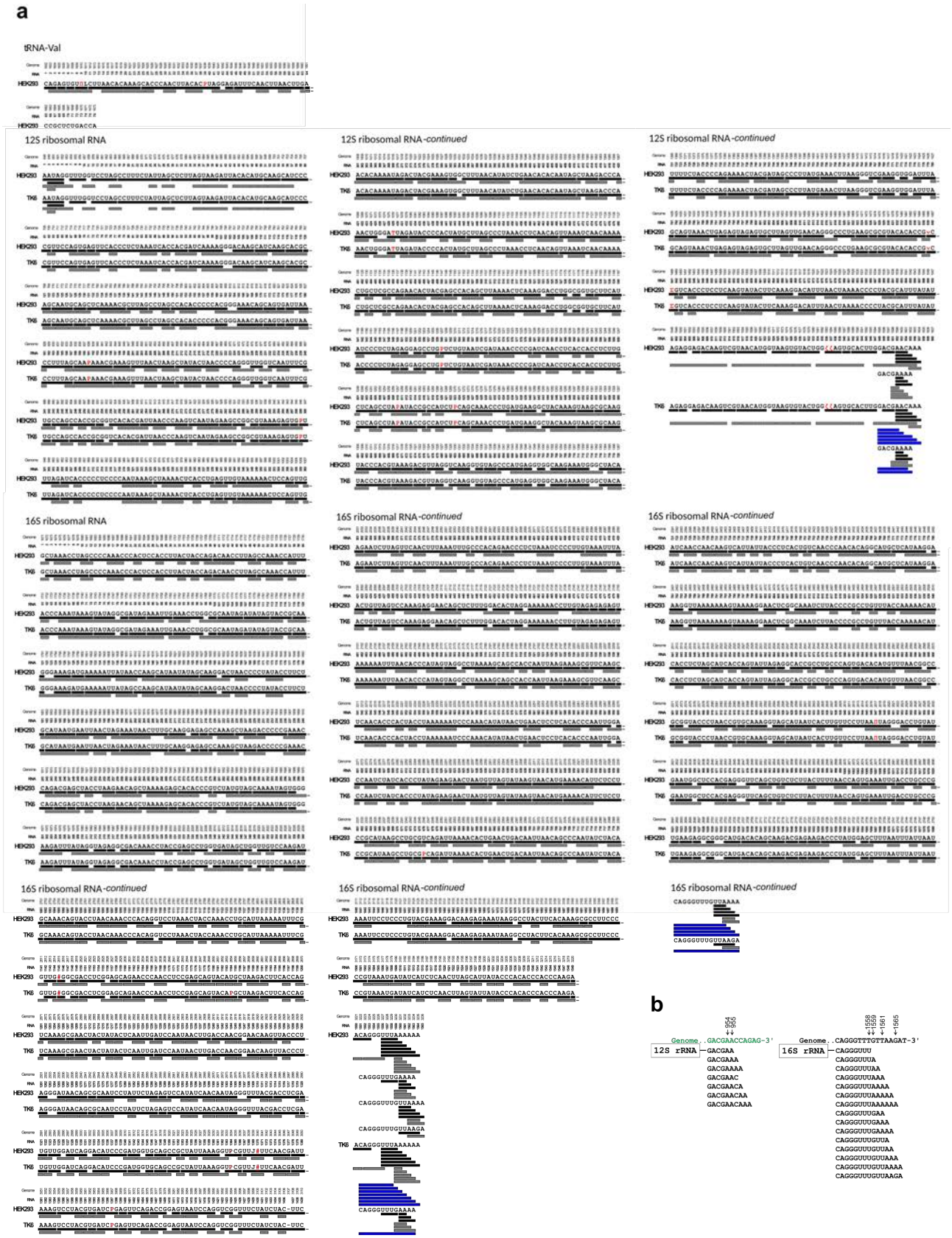

Supplementary Fig. 4: Complete rRNA sequence showing rRNA modifications determined by SILNAS.

a, The complete sequence (numbered according to NC_012920.1) and modifications of the human mitochondrial rRNAs and the fragments used for the structural analysis. Digestion fragments produced by RNase T1 (Black solid); RNase A (black shaded bars) and RNase H (Blue solid bars) are indicated. All fragments were identified by Ariadne software (see Methods). Modified

nucleotides (red letters) and their abbreviations are summarized as follows: P, pseudouridine; Π, 1-methyladenosine; ζ, N6,N6-dimethyladenosine; ν, N4-methylcytidine; Σ, 5-methylcytidine; #, 2′-O-methylguanosine; L, N2-methylguanosine; J, 2′-O-methyluridine; T, 5-methyluridine. **b,** 3' end of 12S and 16S mt-rRNAs show hetero sequences. Mitochondrial genome sequence (NC_012920.1) around 3' end of 12S and 16S are indicated as green text. The transcription termination points are indicated with the residue number and arrow. The hetero 3' end of 12S and 16S mitochondrial rRNAs detected in this study are shown in plain text.

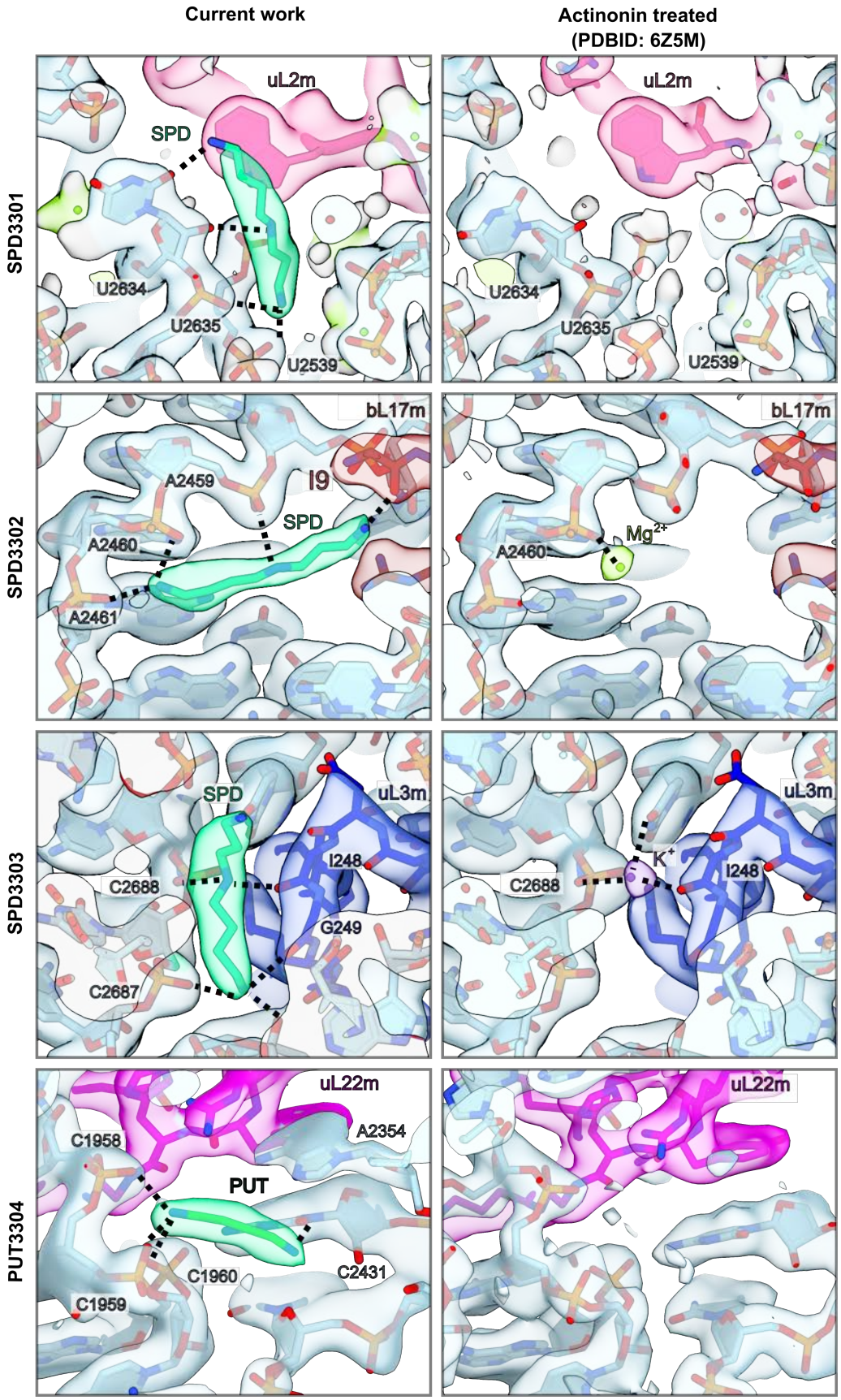

Supplementary Fig. 5: Comparison of polyamine densities with antibiotic-treated cells (PDB ID 6ZM5). Densities (colored by chain) corresponding to spermidine and putrescine are absent upon antibiotic treatment [71]. Absence of putrescine is further associated with a conformational rearrangement of the residue A2354. Interactions are shown with dashed lines.

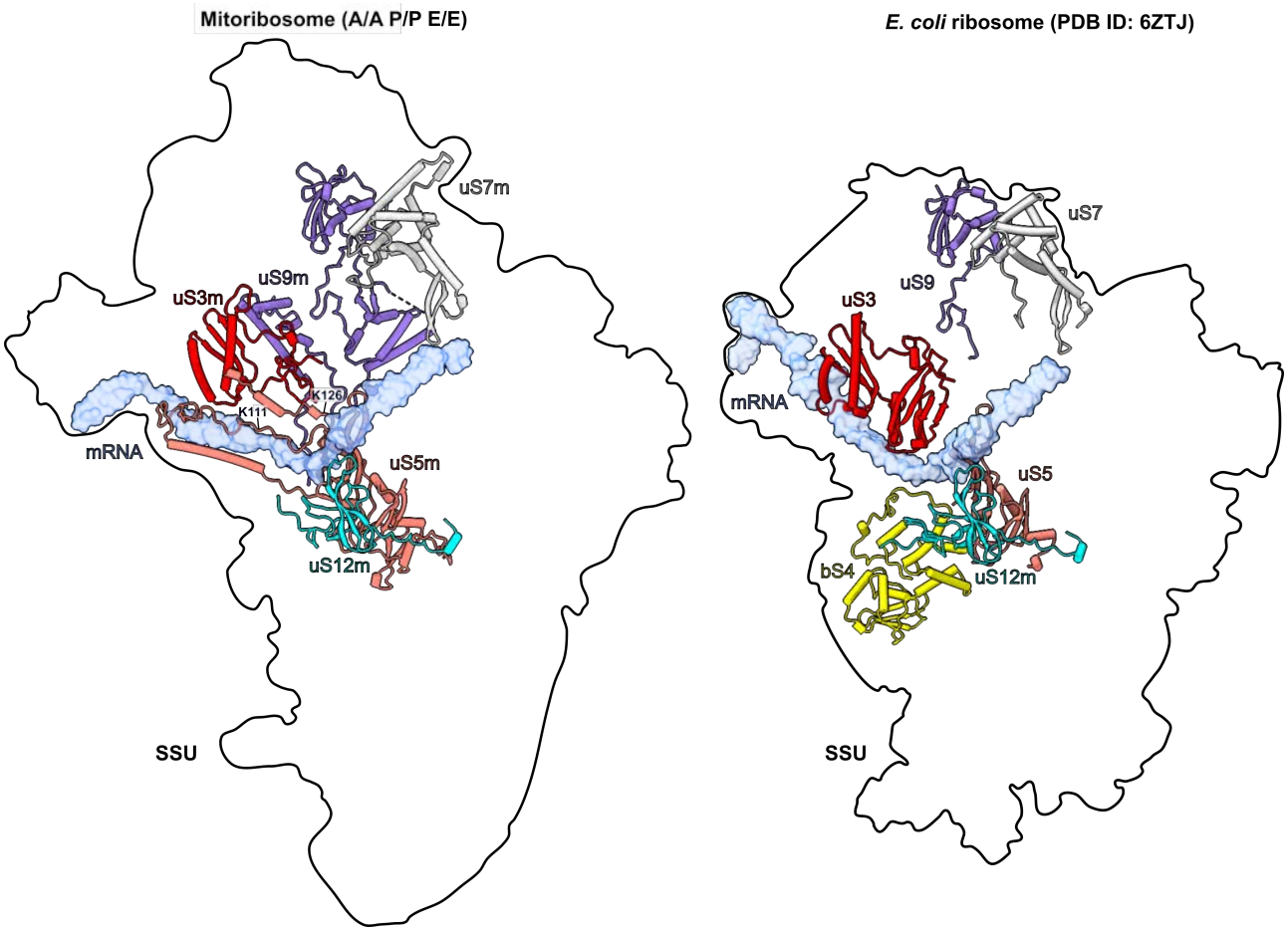

Supplementary Fig. 6: Comparison of protein elements involved in mRNA binding with *E. coli*.

Proteins uS5m, uS7m, uS9m and uS12m (cartoon), mRNA (light-blue surface) from the mitoribosome (left) compared with their bacterial counterparts from *E. coli* [66] (PDB ID 6ZTJ; right). The residues K111 and K126 mark the poly-basic stretch of uS5m. Mitochondria-specific extensions of uS5m and uS9m are positioned along the mRNA channel.

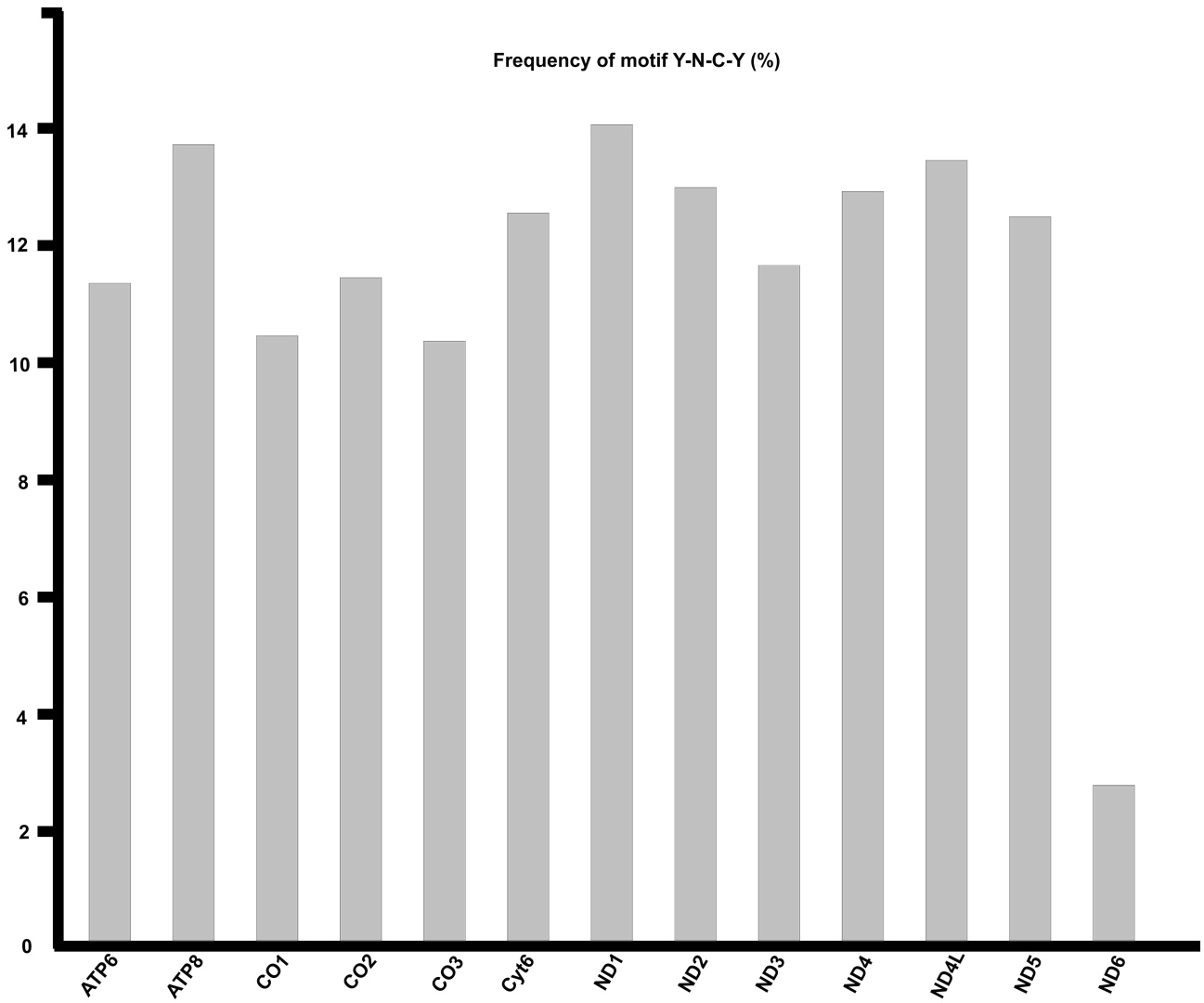

Supplementary Fig. 7: Frequency of Y-N-C-Y motif in the human mitochondrial mRNA transcripts.

Percentage frequency of Y-N-C-Y motif in each of the 13 mitochondrial mRNAs (light grey bars).

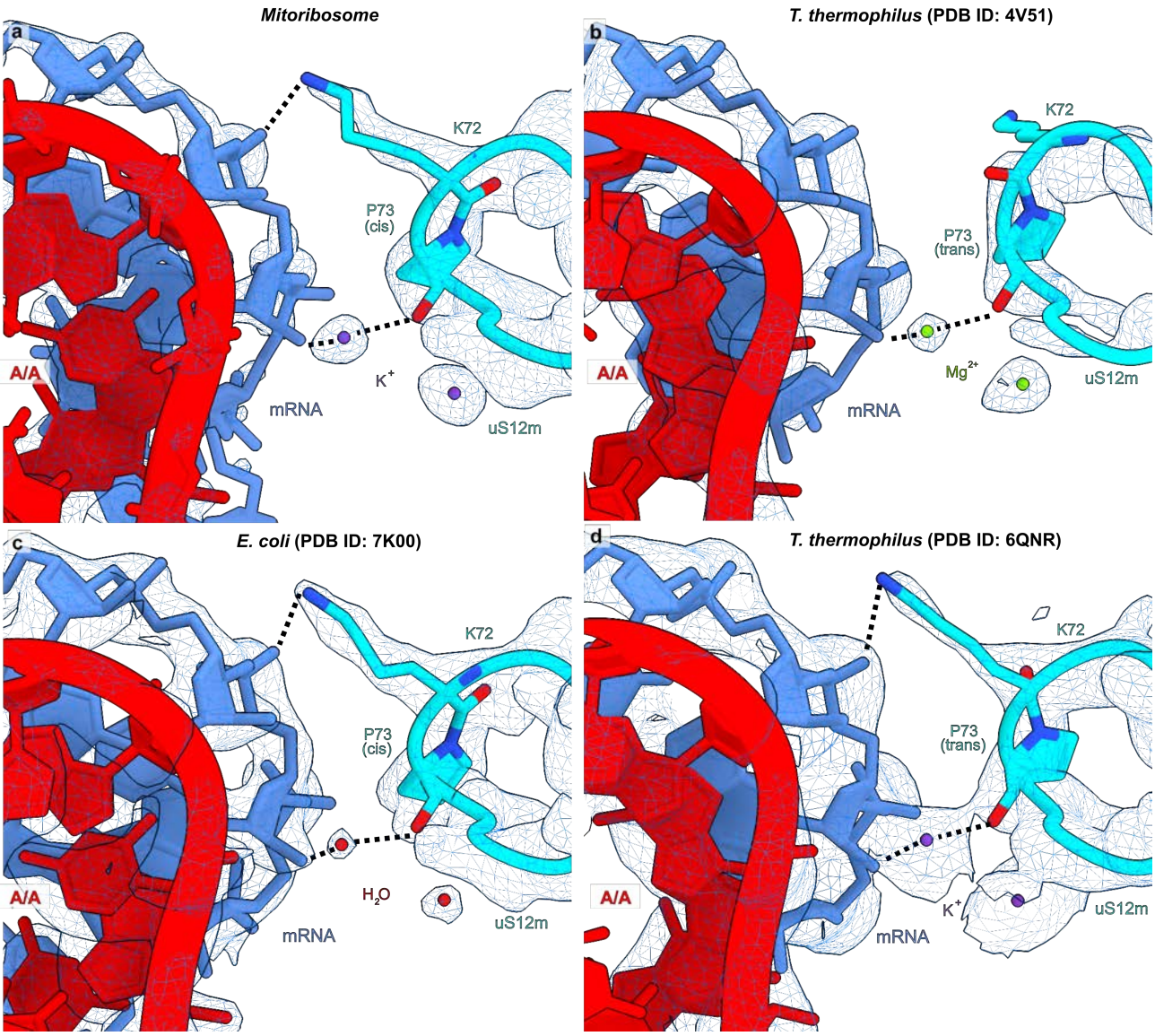

Supplementary Fig. 8: Interactions of uS12m with codon in the A-site.
a, In the mitoribosome at 2.2 Å resolution, P73 is in *cis*, and it coordinates a K^+ ion. K72 side-chain interacts with U9 of the A-site codon. **b,** In *T. thermophilus* ribosome (PDB ID 4V51) at 2.8 Å resolution [52], the densities are assigned as Mg^{2+}, P73 is in *trans*, and K72 is pointing away from the A-site codon. **c,** In *E. coli* ribosome (PDB ID 7K00) at 2.0 Å resolution [48], two water molecules have been modeled, and P73 is in *cis*. **d,** In *T. thermophilus* ribosome (PDB ID 6QNR) at 3.1 Å resolution [53], the densities were assigned as K^+ based on long wavelength X-ray diffraction.

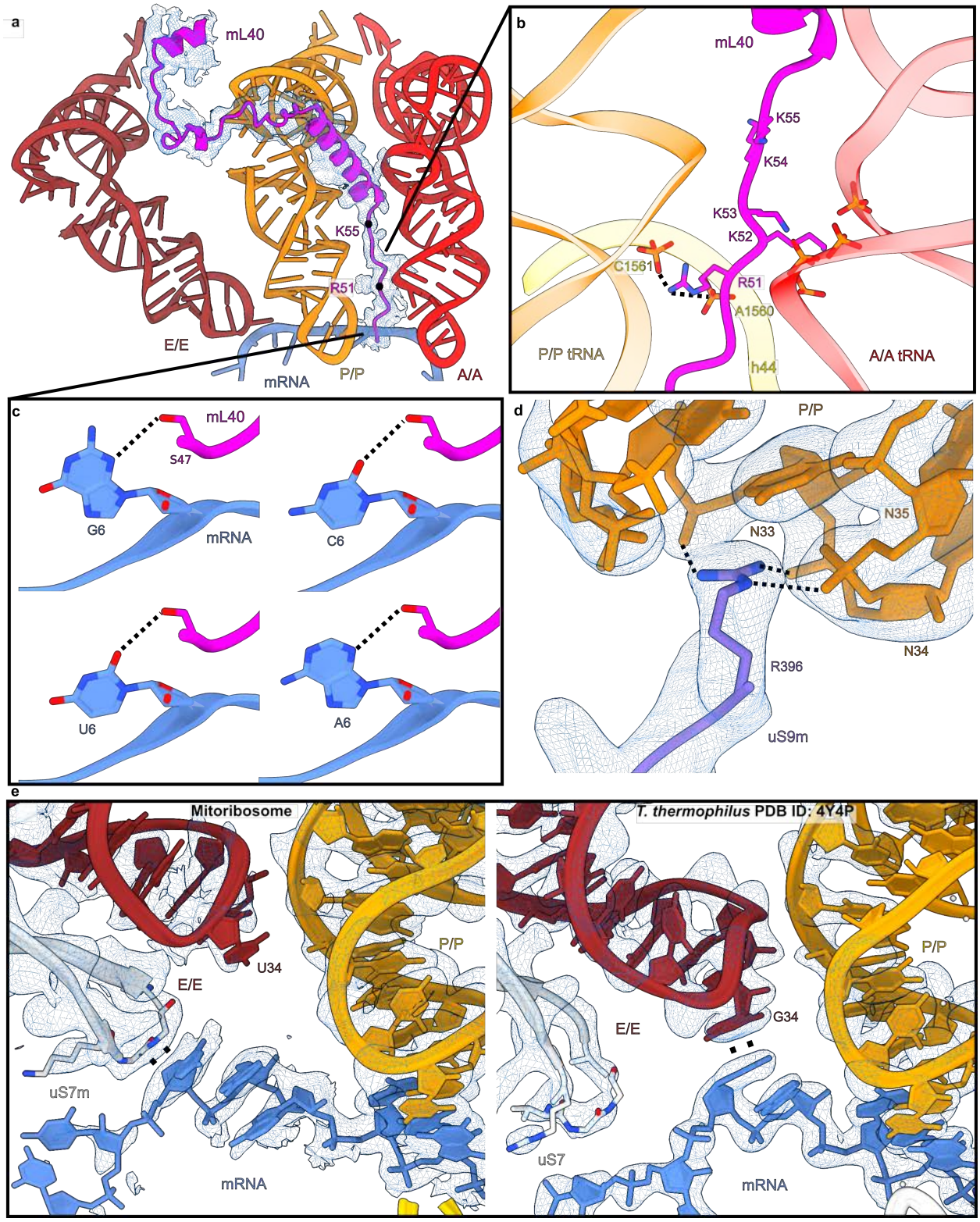

Supplementary Fig. 9: Mitoribosomal proteins involved in mRNA binding.
a, N-terminal region of mL40 lodged between A- and P-tRNA. **b,** basic residues 51-55 of mL40 interact with tRNA phosphate backbone. R51 forms salt bridges with A1560 and C1561 phosphates in h44. **c,** The mRNA residue at position 6 is mutated in Coot v0.9 to depict potential H-bond between S47 side chain and base regardless of base identity. **d,** uS9m C-terminal residue R396 interact with P/P-tRNA anticodon stem-loop. **e,** E-tRNA does not directly interact with mRNA in the mitoribosome. Instead, Gly164 and Gly165 of uS7m stack against mRNA nucleotide base. This is in contrast to the bacterial ribosome [62] (PDB ID 4Y4P) where E-tRNA nucleotide at position 34 stacks with mRNA nucleotide base.

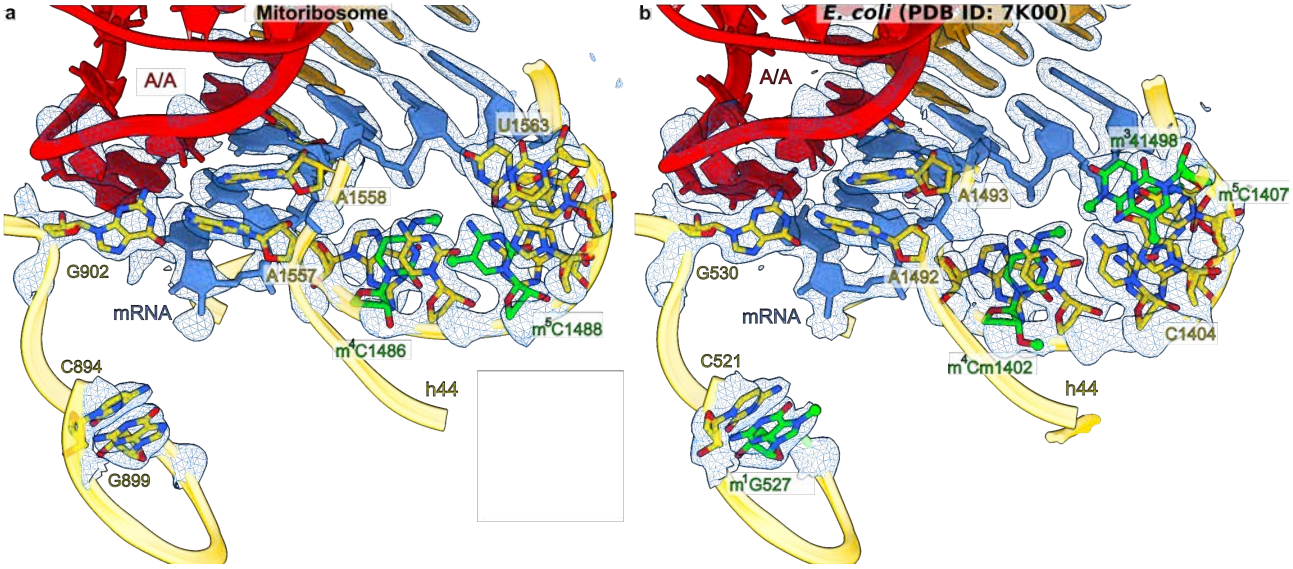

Supplementary Fig. 10: mRNA-rRNA interactions in the decoding center and roles of modifications.

a, Mitoribosome in the classical state: rRNA yellow, mRNA blue, tRNA red, modified nucleotides are labeled and colored lime, cryo-EM density in blue mesh. **b,** *E. coli* ribosome [48] (PDB ID 7K00), the same color scheme as in (a). Differences are observed along the mRNA codons: m^4C1486 (methylated $m^4Cm1402$ in *E. coli*); m^5C1488 (unmodified C1404 in *E. coli*), U1563 (N3-methylated m^3U1498 in *E. coli*). Conserved nucleotides at the decoding center G902, A1557, A1558 interact directly with A-site tRNA anti-codon, equivalent to the corresponding residues G530, A1492 and A1493 in *E. coli*.

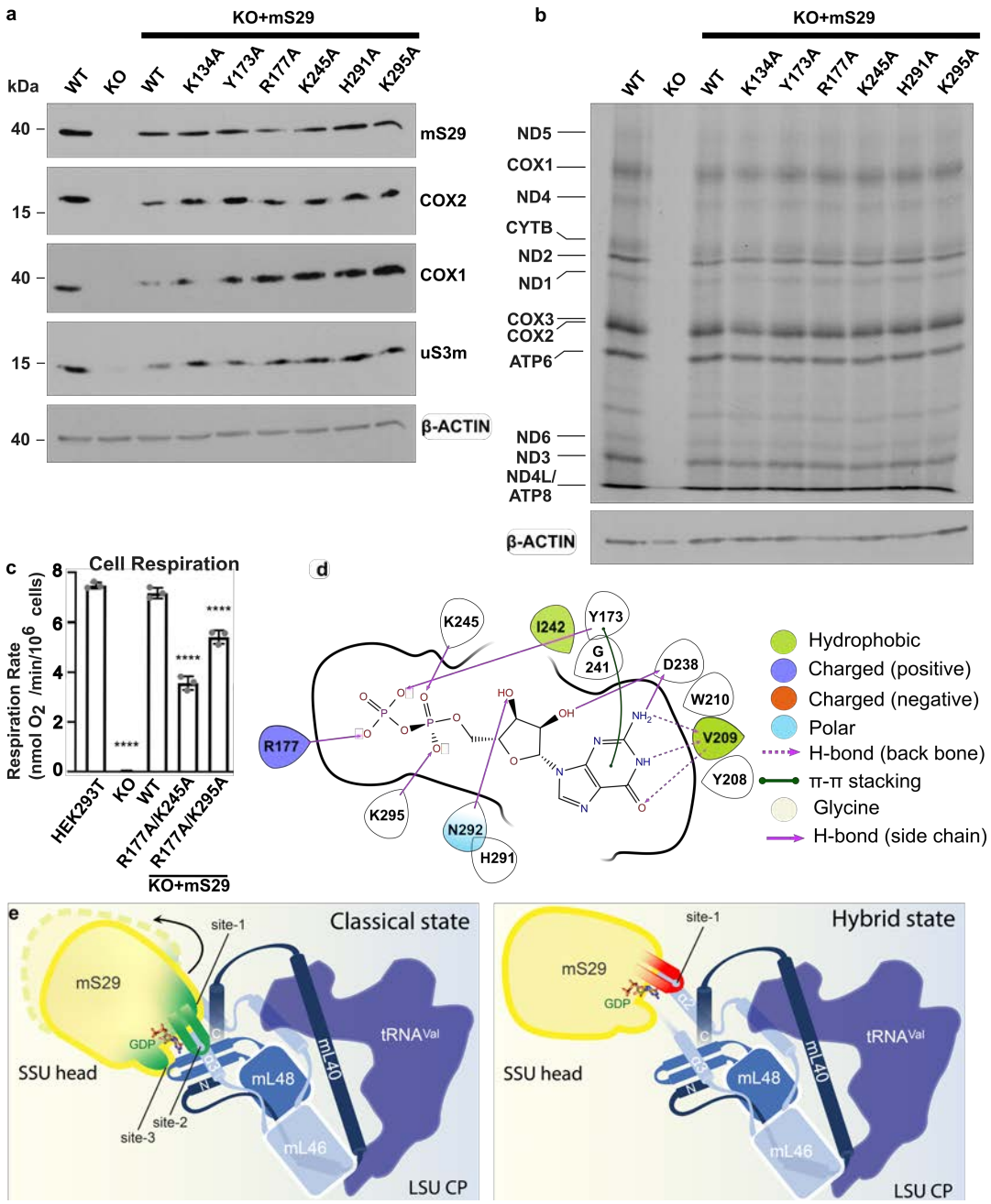

Supplementary Fig. 11: Analysis of nucleotide binding by mS29 and its role in mitoribosome function.

a, Immunoblot analysis comparing steady-state levels of proteins using whole cell protein lysates from HEK293T (WT), *mS29*-KO (KO), and *mS29*-KO cells stably expressing either WT mS29 or single mutants in the ATP binding site (K134A) or GDP binding site (Y173A, R177A, K245A, H291A, K295A) under an attenuated CMV6 promoter (Δ5pCMV6). COX1 and COX2 were used as surrogates of mitoribosome function, uS3m as a control for the SSU, and β-ACTIN as a loading control. Single mutations of mS29 did not have an effect on the steady-state levels of mitochondrial proteins. **b,** Metabolic labeling of mitochondrially translated peptides in whole cells from the indicated cell lines using ^{35}S-methionine for 15 min. Immunoblotting for β-ACTIN was used as a loading control. Newly synthesized peptides are identified on the left. **c,** Cyanide-sensitive endogenous cell respiration rate measured polarographically using a Clark electrode in the indicated cell lines. Cell respiration rates are presented as nmol of O_2 consumed per minute per one million cells. Data represents the mean ± SD of three independent repetitions. **d,** 2D diagram of GDP interactions. **e,** Schematic depiction of intersubunit contacts mediated by mS29.

	Monosome (consensus) PDB: 7QI4 EMD-13980	Monosome (A/A P/P E/E) PDB: 7QI5 EMD-13981	Monosome (A/P P/E) PDB: 7QI6 EMD-13982
Data collection and processing			
Electron microscope	Titan Krios	Titan Krios	Titan Krios
Camera	K2 Summit (counting mode)	K2 Summit (counting mode)	K2 Summit (counting mode)
Magnification	165,000	165,000	165,000
Voltage (kV)	300	300	300
Electron exposure (e^{-}/Å^2)	29–32	29–32	29–32
No. of frames	20	20	20
Defocus range (μm)	−0.6 to −2.8	−0.6 to −2.8	−0.6 to −2.8
Pixel size (Å)	0.83	0.83	0.83
Symmetry imposed	C_1	C_1	C_1
Final particle number (no.)	656,846	82,522	20,134
Map resolution (Å) (Overall/ LSU-body/ CP/ L10-L12-stalk/ L1-stalk/ SSU-body/ SSU-head/ mS39/ SSU-tail/ mS39-LRPPRC-SLIRP)	2.21/ 2.08/ 2.36/ 2.38/2.89/ 2.31/ 2.36/ 2.45/ 2.44/ −	2.63/ 2.44/ 2.78/ 2.84/3.20/ 2.75/2.72/ 2.93/ 2.91/ −	2.98/ 2.84/ 3.25/3.29/3.53/3.07/3.03/3.47/3.39/ −
FSC threshold	0.143	0.143	0.143
Map resolution range (Å)	1.9-8.0	2.1-8.0	2.4-8.0
Refinement			
Initial model used (PDB code)	6ZSG, 6RW4	6ZSG, 6RW4	6ZSG, 6RW4
Model resolution (Å)	2.10	2.50	2.80
Model to map CC (CC_{volume})	0.84	0.84	0.81
FSC threshold	0.5	0.5	0.5
Map-sharpening *B* factor (Å^2) (Overall/ LSU-body/ CP/ L10-L12-stalk/ L1-stalk/ SSU-body/ SSU-head/ mS39/	-38/ -34/ -53/-55/-74/ -43/ -45/ -52/ -52/ −	-36/ -28/ -52/-53/-60/ -39/ -42/ -51/ -51/ −	-42/ -21/ -50/-59/-40/ -35/ -49/ -64/ -57/ −
Model composition			
Non-hydrogen atoms	187689	189567	183520
Hydrogen atoms	152459	154149	153182
Protein chains	88	88	88
RNA chains	7	7	6
Protein residues (non-modified/ *N*-acetylAla/ *N*-acetylSer/ *N*-acetylThr O^1-methylisoAsp)	14790/3/1/1/1	14891/3/1/1/1	14879/3/1/1/1
RNA residues (non-modified/ mG/ mU/ m^1A/ m^2G/ψ /m^4C/ m^5C/ m^5U/ $m^6{}_2A$)	2750/2/ 1/ 2/ 1/ 2/ 1/ 1/ 1/ 2	2814/2/ 1/ 2/ 1/ 2/ 1/ 1/ 1/ 2	2744/ 2/1/ 2/ 1/ 2/ 1/ 1/ 1/ 2
Ligands (ATP/ GDP/ NAD/ 2Fe-2S/ spermine/ spermidine/ putrescine)	1/ 1/ 1/ 3 /1 /4/ 1	1/ 1/ 1/ 3 /1 /4/ 1/	1/ 1/ 1/ 3 /1 /4/ 1
Ions (Zn^{2+}/ K^+/ Mg^{2+})	3/ 54/ 206	3/ 54/ 208	3/ 54/ 202
Waters	8,001	7,714	3,304
Mean atomic *B*-factor (Å^2)			
Protein	42.146	49.50	33.04
RNA	41.81	45.12	32.94
Ligand	27.34	26.81	16.35
Water	25.96	24.50	11.57
Validation			
Ramanchandran plot (%)			
Outliers	0.03	0.03	0.02
Allowed	1.45	1.50	1.54
Favored	98.52	98.47	98.44
Clash score	1.48	2.20	2.03
RMSD			
Bonds (Å)	0.002	0.004	0.002
Angles (°)	0.4531	0.457	0.434
Rotamer outliers (%)	0.00	0.00	0.00
C_β outliers (%)	0.00	0.00	0.00
CaBLAM outliers (%)	0.85	0.77	0.81

Supplementary Table 1: Data collection and model statistics.